iLIVER 1 (2022) 252–264

Contents lists available at ScienceDirect

iLIVER

journal homepage: www.journals.elsevier.com/iliver

Review

Artificial intelligence-based ultrasound imaging technologies for hepatic diseases

Longfei Ma [a,1], Rui Wang [a,1], Qiong He [a], Lijie Huang [a], Xingyue Wei [a], Xu Lu [b], Yanan Du [a], Jianwen Luo [a,*], Hongen Liao [a,*]

[a] Department of Biomedical Engineering, School of Medicine, Tsinghua University, Beijing, 100084, China
[b] Graduate School at Shenzhen, Tsinghua University, Shenzhen, 518055, Guangdong, China

ARTICLE INFO

Keywords:
Artificial intelligence
Ultrasound imaging
Hepatic diseases
Diagnosis and treatment

ABSTRACT

Ultrasound (US) imaging is a non-invasive, real-time, economical, and convenient imaging modality that has been widely used in diagnosing and treating hepatic diseases. Artificial intelligence (AI) technology can predict or make decisions based on the experience of clinical experts and knowledge obtained from training data. This technology can help clinicians improve the detection efficiency and evaluate hepatic diseases, promote clinical treatment of the liver, and predict the response of the liver after treatment. This review summarizes the current rapid development of US technology and related AI methods in the diagnosis and treatment of hepatic diseases. Covered topics include steatosis grading, fibrosis staging, detection of focal liver lesions, US image segmentation, multimodal image registration, and other applications. At present, the field of AI in US imaging is still in its early stages. With the future progress of AI technology, AI-based US imaging can further improve diagnosis, reduce medical costs, and optimize US-based clinical workflow. This technology has broad prospects for application to hepatic diseases.

1. Introduction

The liver is the largest abdomen organ and plays a crucial role in human metabolism, protein synthesis, and clearance of toxins [1]. Maintaining its health and protecting it from liver diseases are vital for human health. Liver diseases are generally divided into diffuse and focal diseases. Diffuse liver diseases spread over a large area or the whole liver, whereas focal liver diseases appear as solid or cystic lesions at one or multiple sites within a portion of the liver. Because ultrasound (US) imaging is non-invasive, real-time, and economical, it is usually the preferred modality for annual physical examinations or for patients with suspected liver disease. Clinicians evaluate the US images and formulate diagnose based on their professional knowledge of imaging patterns associated with different liver disorders, including echo intensity and texture, shape, and contour of lesions [2]. However, image evaluation relies heavily on the subjective judgments and experience of individual clinicians, which may lead to large variability across clinicians and reduce diagnostic reliability.

Artificial intelligence (AI) has been introduced into the medical field to help clinicians with diagnosis and treatment, and for the development of computer-aided diagnosis (CAD) systems. Promising results have been achieved in recent years [3,4]. A major branch of AI is machine learning, which can be generally defined as a mathematical algorithm that makes predictions or decisions based on the experience of clinical experts and knowledge learned from training data [5]. Two main categories of machine learning are supervised learning, which requires annotated data as input and output for training, and unsupervised learning, which explores inner connections and patterns of input data and requires no annotations as prior knowledge. Common supervised learning algorithms include support vector machines (SVM), naive Bayesian, decision tree, random forest, k-nearest neighbor, logistic regression, linear discriminant analysis, quadratic discriminant analysis, kernel discriminant analysis, multilayer perceptron, extreme gradient boosting, adaptive boosting, extreme learning machine, and probabilistic neural network (PNN). Typical unsupervised learning algorithms are k-means clustering and principal component analysis. These machine learning algorithms have

* Corresponding author.
E-mail addresses: luo_jianwen@tsinghua.edu.cn (J. Luo), liao@tsinghua.edu.cn (H. Liao).
[1] These authors contributed equally to this work.

https://doi.org/10.1016/j.iliver.2022.11.001
Received 27 August 2022; Received in revised form 13 October 2022; Accepted 1 November 2022
Available online 16 November 2022
2772-9478/© 2022 The Author(s). Published by Elsevier Ltd on behalf of Tsinghua University Press. This is an open access article under the CC BY-NC-ND license (http://creativecommons.org/licenses/by-nc-nd/4.0/).

been widely used as classifiers after extracting image features either manually or via deep neural networks (DNNs) [6,7]. DNN is the core algorithm of deep learning, which is an emerging and popular branch of machine learning. Deep learning utilizes a neural network with tens of layers, or even deeper structures, to learn the latent mapping from input to output. This approach can handle a variety of tasks and generate outputs of any desired data format such as values, words, and images [8]. At the same time, the universality and flexibility of DNNs come at the cost of heavy reliance on the training data: DNN performance usually depends on dataset size, quality, and distribution. Therefore, massive datasets of medical images represent ideal training material, and deep learning can offer much-needed assistance to a wide range of clinical applications. Convolutional neural networks (CNNs) are commonly used DNNs in medical image analysis. Popular examples include the visual geometry group network (VGGNet), Inception, ResNet, U-Net, GoogLeNet, DenseNet, and AlexNet. These networks have shown an excellent performance in the field of natural image processing, and can be adapted to medical image tasks either by fine-tuning or by training from scratch [9].

The majority of AI-based medical image analysis research has focused on medical images acquired from magnetic resonance imaging (MRI), computed tomography (CT), and radiography, owing to their standard view and clear anatomical delineation. Consequently, relevant reviews have mainly focused on research on MRI and CT images [10,11]. However, US imaging benefits from multimodal data from B-mode imaging, elastography, Doppler imaging, and contrast-enhanced imaging, and shows unique advantages in the diagnosis, treatment, and prognosis of liver diseases. There have been attempts to combine AI technology with multimodal US data to improve the diagnosis or prediction performance compare with that achieved by clinicians or traditional methods. To the best of our knowledge, however, there is a lack of systematic reviews on the application of AI in US imaging of the liver.

To cover relevant articles as extensively as possible, we retrieved records from the Web of Science database between January 2017 and September 2022. Keywords were US, AI, machine learning, deep learning, neural network, liver, hepatic, and hepato. We initially retrieved 570 articles. Next, we read abstracts of all articles and excluded literature according to the following criteria:

(1) Exclude articles that are not available in full text;
(2) Exclude articles written in a language other than English;
(3) Exclude descriptive articles such as letters, review articles, and those focused on research progress and opportunities;
(4) Exclude articles for which US imaging was not the main modality for diagnosis and treatment of the liver;
(5) Exclude articles focused only on image processing techniques or neural network architectures because our focus is specifically on the applications of US imaging and AI to the liver.

We retained 196 articles consistent with the scope of this review (Fig. 1).

In this review, we aim to provide a thorough categorization and summary of existing research on AI-based diagnosis and treatment of the liver combined with US imaging, and propose some perspectives on future challenges in this area of research. The rest of this study is arranged as follows. First, Section 2 introduces five main US imaging modes used in liver applications. Then, Section 3 categorizes and discusses the applications of US imaging to hepatic diseases. Finally, Sections 4 and 5 summarize challenges, prospects, and conclusions.

2. Imaging mode

2.1. Brightness mode imaging

Brightness mode (B-mode) is the most frequently used mode in US examinations. This mode delivers clear delineation of the anatomical structure by converting the log-compressed intensity of US echo to brightness across a two-dimensional (2D) image. For convenience of description, echo intensity is graded as high level, medium level, low level, and echo-free, and corresponding image regions are described as hyperechoic, isoechoic, hypoechoic, and anechoic, respectively. The echo intensity of human tissues and body fluids shows some regularities [12]. For example, homogeneous fluids like bile and blood are usually anechoic or hypoechoic, homogeneous tissues like parenchyma are isoechoic, and calcification and hemangioma (HEM) are usually hyperechoic. Morphological parameters measured from B-mode images, such as size, area, shape, and aspect ratio, can support effective diagnosis of organ abnormalities and solid lesions [13,14]. Radiologists are able to recover abundant anatomical information from B-mode images, allowing them to formulate diagnostic US reports based on their professional knowledge of sectional anatomy and pathological anatomy [15].

Beyond the direct information available from the image, texture features extracted from the image can also provide lots of hidden information for diagnosis [16]. Texture analysis methods mainly include statistical analysis and domain transformation. Texture features derived from statistical analysis include average intensity, standard deviation, skewness, kurtosis, entropy, gray-level co-occurrence matrix, gray-level run-length matrix, local binary pattern, and histogram of oriented gradient. These features can be used to quantify the spatial distribution of pixel intensities in the B-mode image. Texture analysis based on domain transformation transforms the B-mode image into other domains, like the frequency domain or the wavelet domain, and extracts features within these domains to obtain a new representation of the image. These features have played an important role in radiomics analysis, and have provided an effective assistance for diagnosis through feature selection and statistical modeling [10,17].

2.2. Doppler imaging

Doppler imaging takes advantage of the Doppler effect associated with US waves, which is caused by moving scatterers (i.e., red blood cells) in the blood vessels. This technique effectively monitors blood flow, including flow velocities and directions relative to the transducer [18]. Common Doppler US imaging technologies include Doppler spectrum, color Doppler flow imaging (CDFI), and power Doppler imaging (PDI). Doppler spectrum measures the distribution of flow velocities over time along the US beam (continuous-wave Doppler spectrum) or within a short-range gate along the US beam (pulsed-wave Doppler spectrum), and does not provide 2D spatial information. CDFI shows the mean velocity of blood flow and the flow direction relative to the transducer of different spatial locations within a region of interest. Flow velocity and direction are typically color-coded and overlaid onto the B-mode image, to provide both blood flow and anatomical information. PDI emphasizes blood volume by color-coding the signal power of blood flow. This approach ignores flow direction, and thus delineates more clearly the structure of blood vessels.

The assessment of hepatic blood flow supports inferences about hepatic physiology and pathology. For example, altered directionality of blood flow in the portal vein suggests the risks of cirrhosis, portal venous hypertension, and thrombosis [19]. Existing literature [20] has systematically illustrated how hepatic parenchymal abnormalities and primary vascular abnormalities can be inferred from US Doppler imaging including Doppler spectrum, CDFI, and PDI. However, many factors can impact hepatic blood flow, including neoplastic and inflammatory conditions. As a consequence, Doppler signatures of the liver cannot act as sole diagnostic criteria.

2.3. Contrast-enhanced US imaging

Common US contrast agents for the current clinical use are microbubbles composed of low-solubility gasses, like sulfur hexafluoride and perfluorocarbon, encapsulated in shells [21]. These specially designed agents not only generate strong echoes at the fundamental frequency and

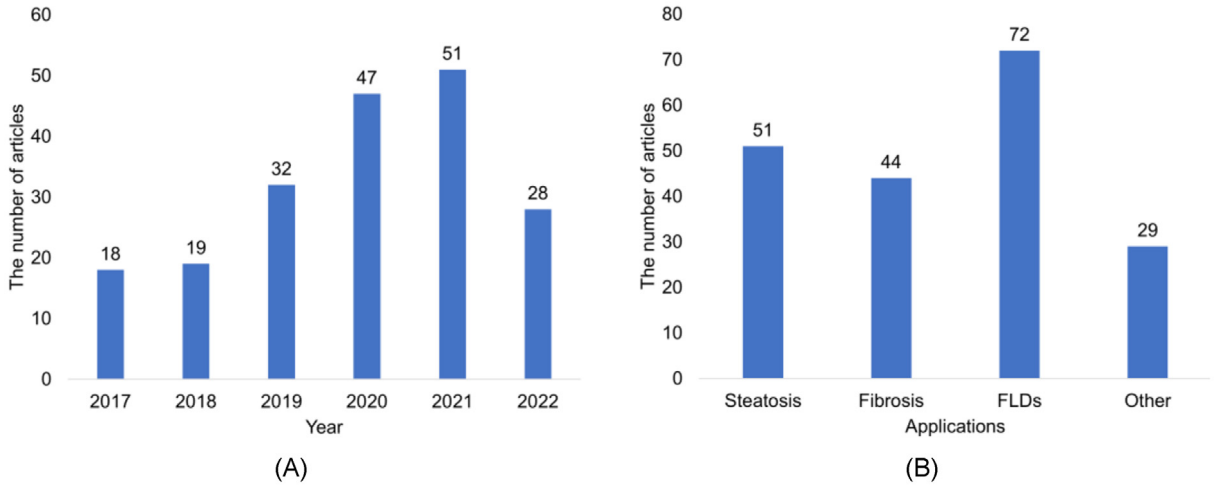


Fig. 1. (A) Number of articles in different years; (B) Number of articles associated with different applications to the liver.

increase the signal-to-noise ratio of the B-mode image but also lead to non-linear oscillations at the second harmonic and increase contrast-to-tissue ratio in the contrast-enhanced US (CEUS) image [22]. Furthermore, the short half-life and intravascular circulation of microbubbles allow for the sequential evaluation of multiple phases and sites of lesions.

Intravenous injection of US contrast agents increases the weak US signal from blood, enhances the detection of blood vessels, and improves the measurement of blood flow [23]. In addition, CEUS imaging of the liver during the arterial phase, portal venous phase, and late phases, is regarded as an effective diagnostic tool for the differentiation of focal liver lesions [24]. Liver-specific US contrast agents like Sonazoid® can also be absorbed by the Kupffer cells and sustained for as long as 1 h, thus allowing for an additional hepatic parenchyma-specific Kupffer phase imaging on CEUS. Most tumors, especially malignant tumors like metastasis, show Kupffer cell reduction. Hypo-enhancement or absent enhancement detected in the Kupffer phase associated with CEUS can be used to distinguish between metastatic lesions and other benign lesions [25].

2.4. Elastography

US elastography assesses and displays tissue elasticity (in terms of Young's modulus or shear modulus) by estimating tissue motion, deformations, or shear wave propagation caused by external (such as compression and vibration) or internal sources (such as acoustic radiation force and physiological movement) [26]. Young's modulus is an inherent biomechanical property mainly determined by the structure and components of tissue, which varies from a few tenths to thousands of kilo-Pascals across different human tissues. The Young's modulus of a tissue can change in the presence of some pathological processes, like fibrosis and cancerization [27]. Therefore, the Young's modulus of liver tissue can serve as an indicator of hepatic diseases like fibrosis and cirrhosis [27].

For liver applications, shear wave elastography (SWE) is the most common technology of ultrasound elastography. This technique relies on shear wave velocity (SWV) to provide a direct measurement of the Young's modulus of the tissue. These two quantities are related by the formula $E = 3\rho c^2$, where E is Young's modulus of the tissue, ρ is tissue density, and c is SWV. Three common SWE techniques are transient elastography (TE), point SWE (pSWE), and 2D-SWE [28]. TE is a one-dimensional measurement technique that applies a transient force perpendicular to the body surface with an external vibration source and estimates the velocity of the shear wave traveling along the force direction on the basis of the resulting one-dimensional echo signal [29]. The pSWE technique measures the average velocity of the shear wave propagating from one boundary to the opposite boundary of a measurement region. The shear wave is generated by the acoustic radiation force focused at a certain depth within the tissue [30]. 2D-SWE utilizes the acoustic radiation force focused at multiple sequential locations, or multiple unfocused US beams arranged in a comb pattern, to generate shear waves traveling across a large region of tissue [31,32]. Therefore, 2D-SWE monitors 2D deformations across the imaging plane, and can generate a color-coded SWV or elasticity map overlaid onto the B-mode image. This image provides far more information than a single measurement from TE and pSWE.

Liver stiffness measurement (LSM) provided by TE has been included in the recommendations and consensus on the diagnosis of chronic liver diseases [33,34]. Patients with non-alcoholic fatty liver disease (NAFLD) are suspected of cirrhosis if LSM $\geq$ 15.0 kPa and fibrosis if LSM $\geq$ 11.0 kPa [33]. Patients with alcoholic liver disease (ALD) are excluded from cirrhosis if LSM $<$ 12.5 kPa and fibrosis if LSM $<$ 9.5 kPa [33]. However, cutoff LSM values for fibrosis and cirrhosis vary in different chronic liver diseases. LSM is usually considered during preliminary diagnosis, but biopsy is still required for accurate diagnosis.

2.5. Quantitative US

We narrowly define quantitative US (QUS) as the ensemble of techniques that exploit backscattered spectra from beamformed radiofrequency (RF) signals to estimate acoustic parameters such as acoustic attenuation, backscatter coefficient (BSC), and speed of sound. B-mode images contain signal magnitude information that is related to the acoustic impedance of the tissue. In contrast, the RF signal carries both magnitude and phase information, allowing for spectral analysis of the signal and estimation of additional acoustic parameters besides acoustic impedance.

An important application of QUS in the liver is the quantification of hepatic steatosis. Acoustic attenuation and BSCs have proved to be highly correlated with the levels of lipids in the liver [35,36]. QUS methods based on attenuation and BSC are capable of detecting and grading the fatty liver [37,38]. In addition, the extraction of useful information from RF signals is not limited to traditional QUS methods, which are mainly based on physical models. Features extracted from RF signals via handcrafted methods or by DNNs have outperformed features extracted from B-mode data in the detection and diagnosis of liver lesions [39,40].

3. Liver applications

3.1. Diagnosis of diffuse liver diseases

A major subtype of diffuse liver disease involves chronic liver diseases with high prevalence all over the world, which affect over 447 million

patients in China [41]. Viral hepatitis, ALD, and NAFLD are the most common chronic liver diseases. The development of these diseases is usually accompanied by steatosis and fibrosis, which are the focus of AI-based diagnosis.

3.1.1. Steatosis grading

Steatosis is a reversible pathological process in which lipids, like triglycerides, accumulate within the cytoplasm of hepatocytes as a consequence of their abnormal lipid metabolism. ALD and NAFLD are the leading causes of steatosis. Other secondary causes include obesity, drugs, hepatitis, and starvation. Steatosis can be graded into normal, mild, moderate, and severe based on liver echo patterns from US scans. "Mild" indicates a minor increase of parenchymal reflectivity. "Moderate" is characterized by an indistinct intrahepatic vessel wall, and by discontinuous diaphragm lines. "Severe" refers to poor penetration of the liver parenchyma and nearly invisible hepatic vessels and diaphragm.

The gold standard for diagnosing steatosis is liver biopsy, which classifies steatosis into four grades S0–S3 based on the percentage of parenchymal hepatic cells with intracellular fat droplets in biopsy tissue samples. S0 indicates normal liver with less than 5% adipose tissue accumulation. S1 indicates mild steatosis with 5%–33% adipose tissue accumulation. S2 indicates moderate steatosis with 34%–66% adipose tissue accumulation. S3 indicates severe steatosis with more than 66% adipose tissue accumulation in the liver. MRI proton density fat fraction (MRI-PDFF), which estimates the percentage of triglycerides in the liver from the density of mobile protons from triglycerides and from mobile water, correlates strongly with the results obtained from biopsy quantification. Therefore, MRI-PDFF has been adopted as a convenient alternative marker for the validation of classifier performance in some studies.

Many researchers are employing traditional machine learning or deep learning strategies for the detection and grading of liver steatosis (Table 1). Most studies take only B-mode images as input to the AI model. Das et al. developed an ensemble classification model based on machine learning to differentiate pediatric NAFLD from healthy liver tissue using features from texture analysis, which outperformed a model based on US intensity-based indices [46]. Neogi et al. proposed a PNN model that relied on a set of anisotropy features from B-mode images for detecting steatosis and achieved near-perfect performance in terms of accuracy and sensitivity [56]. Sharma et al. described a CAD system for the classification of fatty and normal liver images, which achieved 95.55% accuracy and 97.77% sensitivity with the 20 best features selected using mutual information feature selection [59]. Salvati et al. proposed a system employing neighborhood component analysis for feature selection and multiple machine learning approaches for the classification of steatosis severity and obtained the best results for the three binary classification tasks $\geq$S1, $\geq$S2, and $\geq$S3 with quadratic discriminant analysis, linear discriminant analysis, and SVM, respectively [60]. Kuppili et al. proposed a reliable extreme learning machine-based CAD system for the stratification of FLD-affected and FLD-unaffected liver images, which achieved superior performance compared with SVM in terms of sensitivity, specificity, accuracy, and area under the receiver operating characteristic curve (AUC) [64].

Besides traditional machine learning approaches, DNN has also been utilized for the automatic assessment of liver steatosis in B-mode images. Constantinescu et al. performed transfer learning with different CNN architectures based on Inception v3 or VGG-16 to detect steatosis and classify normal versus fatty liver images, and yielded a classification performance of over 90% [47]. Chou et al. compared the performance of five pre-trained CNN models in classifying the severity of fatty liver and identified ResNet-50 v2 as the best model with AUC values of 0.974, 0.971, 0.981, 0.985, and 0.996 for mild, moderate, severe, normal, and clinically abnormal, respectively [48]. Che et al. designed a multi-feature CNN architecture taking the original B-mode images, their corresponding local filtered images, and radial symmetry transformed images as input. They then tested various fusion strategies to improve the accuracy of NAFLD prediction [49]. Reddy et al. proposed a CNN architecture for the detection and classification of NAFLD texture with an overall accuracy of 93.5% and partial accuracy values of 100%, 95.3%, 92.8%, and 85.7% for S3, S2, S1, and S0 categories, respectively [62]. Byra et al. used the Inception-ResNet v2 CNN to extract high-level features from sequences of B-mode images and classified images containing fatty liver with SVM. The CNN obtained a higher AUC (0.977) than the hepatorenal index method (0.959) and the gray-level co-occurrence matrix method (0.893) [63].

A few studies have explored the feasibility of other data types, like RF data, for grading steatosis. Sanabria et al. directly compared the efficacy of B-mode data versus RF data as training datasets for CNN-based grading of NAFLD steatosis, and showed that RF data supported superior classification accuracy [40]. Cao et al. compared the diagnostic ability of the envelope signal value, grayscale signal value, and deep-learning index in assessing the severity of NAFLD. They obtained superior sensitivity and specificity for discriminating between moderate and severe NAFLD using the deep-learning index [53]. Liu et al. applied pattern recognition in the time domain and in the frequency domain of RF signals to grade fatty liver. Features including the mathematical expectation, the multi-fractal spectrum width, the low-frequency wavelet coefficients mean, and the wavelet modulus maximum mean are extracted from the selected regions of interest for classification. They achieved diagnostic accuracy values of 92.0%, 88.0%, 90.0%, and 94.0% for normal, mild, moderate, and severe fatty liver, respectively [57]. Sanabria et al. devised a multi-parametric model to learn quantification of steatosis from B-mode, SWE, and RF data. The multi-parametric model achieved superior regression coefficient of 0.87 with MRI-PDFF and outperformed all uni-parametric models [50].

3.1.2. Fibrosis staging

Liver fibrosis is commonly observed in many chronic liver diseases that subsequently progress to cirrhosis. Fibrosis is a histologically reversible process that the extracellular matrix (glycoprotein, proteoglycans, and collagen) excessively deposits and replaces parenchyma cells after the liver suffers from serious injuries. The gradual loss of parenchyma cells leads to a developmental process of liver dysfunction. Further development of fibrosis may cause hepatic structural disorder, nodular regeneration, and pseudolobule formation.

Liver biopsy is the gold standard for diagnosing fibrosis. Many scoring systems have been proposed to assess disease progression semi-quantitatively based on histopathological findings. The commonly used scoring systems for pathological diagnosis and data annotations of AI-based classification are the Scheuer and METAVIR scoring systems. The Scheuer scoring system divides hepatic fibrosis into five stages from S0 to S4. S0 indicates no fibrosis. S1 indicates expansion of the portal area. S2 indicates that there is portal fibrosis and the formation of fiber septa. S3 refers to the existence of fiber septa with lobular structural disorder. S4 is probable or definite cirrhosis. The METAVIR scoring system classifies hepatic fibrosis into five stages from F0 to F4. F0 indicates no fibrosis. F1 indicates portal fibrosis without fiber septum. F2 refers to portal fibrosis with few fiber septa. F3 is septa fibrosis and F4 is cirrhosis.

Some general clinical scoring systems assess hepatic fibrosis based on available clinical and laboratory variables. Three representative scoring systems are the NAFLD fibrosis score, fibrosis-4 (FIB-4), and the aspartate aminotransferase to platelet ratio index (APRI). These scoring systems calculate a score using an empirical formula that incorporates variables like age, body mass index (BMI), hyperglycemia, platelet count, albumin, aspartate aminotransferase (AST), and alanine aminotransferase (ALT). Comparing the score with a series of cutoff values indicates patients with a low- or high-risk for significant fibrosis (F0–F2), advanced fibrosis (F3–F4), or cirrhosis (F4). The result is only indicative and further examination is required if the score falls within an undefined range.

Several studies have investigated the detection and stage assessment of liver fibrosis with traditional machine learning or deep learning strategies (Table 2). Nearly half of the studies still focus on classification from B-mode images only. Feng et al. proposed a CNN that implements multi-scale information extraction and attention integration, and

Table 1
Grading of steatosis using US imaging and AI.

Year	Data type	Method	Best performance	Ref.
2022	RF signals	CNN	Average: 0.989 ACC, 0.998 AUC	[42]
2022	B-mode	ResNet-18	≥Mild: 0.85 AUC ≥Moderate: 0.91 AUC ≥Severe: 0.93 AUC	[43]
2022	B-mode	ResNet-50	Spearman correlation coefficient with PDFF: 0.81 Pearson's correlation coefficient with PDFF: 0.78 PDFF ≥ 5%: 0.91 AUC, PDFF ≥ 10%: 0.86 AUC	[44]
2021	B-mode	DeepLabv3+ + Inception v3	Non-cropped data: 95.38% ACC, 95.77% SEN, 95.09% SPE Cropped data: 99.91% ACC, 99.78% SEN, 100.0% SPE	[45]
2021	B-mode	SVM/MLP/XGBoost	SVM: 0.971 AUC, MLP: 0.941 AUC XGBoost: 0.961 AUC, Combined: 0.969 AUC	[46]
2021	B-mode	Inception v3	93.23% ACC, 88.9% SEN, 96.6% PRE, 0.93 AUC	[47]
2021	B-mode	ResNet-50 v2	84.1% ACC, 83.8% SEN, 94.8% SPE, 0.840 F1 score	[48]
2021	B-mode	ResNet	Early-fusion model: 95.3% ACC, 0.98 AUC Middle-fusion model: 97.8% ACC, 1.00 AUC Late-fusion model: 97.0% ACC, 0.99 AUC	[49]
2020	B-mode, RF signals, SWE	MLP + QA	Pearson correlation coefficient with PDFF: r = 0.88	[50]
2020	B-mode, RF signals	CNN	≥S1(ACC): 86.4% patches, 96.2% views, 100% patients ≥S2(ACC): 75.1% patches, 84.6% views, 87.5% patients ≥S3(ACC): 73.2% patches, 84.6% views, 87.5% patients	[40]
2020	RF signals	CNN	Classification: 96% ACC, 97% SEN, 94% SPE, 0.98 AUC Pearson correlation coefficient with PDFF: r = 0.85	[51]
2020	RF signals	VGG-16	≥Mild: 70% ACC, 73.18% SEN, 60.00% SPE, 0.71 AUC ≥Moderate: 80% ACC, 63.25% SEN, 74.82% SPE, 0.75 AUC ≥Severe: 97% ACC, 85.23% SEN, 84.12% SPE, 0.88 AUC	[52]
2020	Envelope signals and grayscale signals	CNN	Normal vs NAFLD: 0.933 AUC Mild vs moderate: 0.692 AUC Moderate vs severe: 0.958 AUC	[53]
2020	B-mode and RF data	Inception + ResNet v2	82% ACC, 0.84 AUC	[54]
2019	B-mode	VGG-16	90.5% PRE, 91.2% SEN, 90.8% F1 score	[55]
2019	B-mode	PNN	99% ACC, 97% SPE, 100% SEN	[56]
2019	RF signals	C-means clustering and backpropagation neural network	Normal: 92.0% ACC; mild: 88.0% ACC Moderate: 90.0% ACC; severe: 94.0% ACC	[57]
2019	B-mode	LR/SVM	Hybrid method: 87.5% ACC, 0.812 Kappa, 0.119 MAE	[58]
2018	B-mode	SVM	95.55% ACC, 97.77% SEN, 93.33% SPE, 0.95 AUC	[59]
2018	B-mode	QDA/LDA/SVM	≥S1: 0.79 YI, 0.91 AUC ≥S2: 0.84 YI, 0.99 AUC ≥S3: 0.8 YI, 0.92 AUC	[60]
2018	B-mode	VGG-16	90.6% ACC, 95% SEN, 85% SPE	[61]
2018	B-mode	CNN	93.5% PRE, 93.45% SEN, 93.3% F-score	[62]
2018	B-mode	ResNet v2 + SVM	96.3% ACC, 100% SEN, 88.2% SPE, 0.977 AUC	[63]
2017	B-mode	ELM	92.4% ACC, 91.3% SEN, 92.1% SPE, 0.92 AUC	[64]

Abbreviations: ACC, accuracy; AUC, area under the curve; CNN, convolutional neural network; ELM, extreme learning machine; MAE, mean absolute error; MLP, multilayer perceptron; LDA, linear discriminant analysis; LR, linear regression; PDFF, proton density fat fraction; PNN, probabilistic neural network; PRE, precision; QA, qualitative assessment; QDA, quadratic discriminant analysis; SEN, sensitivity; SPE, specificity; SVM, support vector machine; XGBoost, extreme gradient boosting; YI, Younden Index.

achieved a classification accuracy of 95.7% on the liver fibrosis dataset [68]. Ruan et al. constructed a multi-scale texture network to assess liver fibrosis. The resulting AUC values significantly outperformed those obtained from APRI and FIB-4 in the identification of significant fibrosis (≥F2) and cirrhosis (=F4) [71]. Lee et al. developed a CNN for the prediction of METAVIR scores and achieved a significantly higher AUC (0.857) for the classification of cirrhosis than the values returned by five radiologists (0.656–0.816) [77]. Acharya et al. performed a 2D contourlet transform and extracted a set of non-linear texture features from the transformed image. The five stages of fibrosis were classified with 91.5% accuracy, 92.2% sensitivity, and 88.9% specificity using only four features as input to the PNN classifier [85].

Some studies detected and segmented the region of interest in advance to improve classification performance. Xu et al. separated the parenchymal region from the high-frequency US image with an autoencoder and a partition-clustering algorithm. They then used a residual neural network to determine the stage of cirrhosis, which outperformed five other state-of-the-art methods [86]. Liu et al. first localized liver capsules within the US images, and then extracted features from patches on, above, and below the liver capsule. When these features were used as input to a CNN classifier, 86.9% accuracy and 0.951 AUC were achieved in the diagnosis of cirrhosis [88]. Saito et al. implemented a system that extracted regions of liver parenchyma with U-Net and classified the stage of fibrosis as F0, F1, F2, F3, or F4 with a regression model based on ResNet-18. Using this approach, the authors obtained a mean Dice coefficient of 0.929 for segmentation, and a mean absolute error of 1.22 for classification [70].

Several researchers have utilized elastography data to reach considerable classification performance. Zhou et al. adopted a CNN based on transfer learning of SWE. Their approach outperformed 2D-SWE, TE, APRI, and FIB-4 in predicting different stages of liver fibrosis [74]. Xue et al. proposed a transfer learning model based on Inception v3 for liver fibrosis classification. Their model analyzed images of grayscale modality (GM) and 2D-SWE-based elastogram modality (EM) and achieved higher accuracy for the multimodal GM + EM configuration compared with GM + LSM, GM alone, EM alone, LSM alone, and biomarkers [75]. Wang et al. developed deep learning radiomics of elastography for quantitative analysis of the heterogeneity in 2D-SWE images. They successfully predicted the stage of liver fibrosis with AUC values of 0.97 for cirrhosis (=F4), 0.98 for advanced fibrosis (≥F3), and 0.85 for significant fibrosis (≥F2) [81]. Lei et al. assessed the stage of liver fibrosis in chronic hepatitis B using feature selection and machine learning methods. Based on TE and acoustical radiation force impulse imaging data, they achieved accuracy values of 90.68% and 93.52% for significant fibrosis (≥F2) and cirrhosis (=F4), respectively [89]. Durot et al. showed that a multivendor SVM model can successfully discriminate between non-significant (<F2)

Table 2
Identification of fibrosis stage using US imaging in combination with AI.

Year	Data type	Method	Best performance	Ref.
2022	B-mode	GAN	≥F3: 0.762 AUC; =F4: 0.835 AUC	[65]
2022	RF signals	ANN	≥F1: 0.88 AUC; ≥F2: 0.53 AUC ≥F3: 0.48 AUC; =F4: 0.85 AUC	[66]
2022	B-mode	ResNet-50	0.901 AUC	[67]
2022	B-mode	VGG-16	95.75% ACC	[68]
2021	Doppler and SWE	ANN	95.8% ACC, 95.4% SEN, 96.2% SPE	[69]
2021	B-mode	CORALNet	1.55 MAE, 1.34 RMSE	[70]
2021	B-mode	DGANet	≥F2: 85.1% SEN, 87.6% SPE, 0.92 AUC =F4: 87.8% SEN, 78.1% SPE, 0.89 AUC	[71]
2021	RF signals	SVM	≥F2: 85.71% F1 score	[72]
2021	B-mode	CNN + MLNN	≥F1: 89.4% ACC, 93.0% SEN, 82.6% SPE, 0.851 AUC ≥F2: 74.2% ACC, 71.4% SEN, 76.3% SPE, 0.793 AUC ≥F3: 68.2% ACC, 75.0% SEN, 66.0% SPE, 0.784 AUC =F4: 65.2% ACC, 80.0% SEN, 62.5% SPE, 0.789 AUC	[73]
2020	SWE	CNN	≥F2: 0.85 AUC; ≥F3: 0.98 AUC; =F4: 0.98 AUC	[74]
2020	B-mode and SWE	Inception v3	≥S2: 87.9% SEN, 83.2% SPE, 0.907 AUC ≥S3: 85.2% SEN, 90.0% SPE, 0.910 AUC =S4: 89.1% SEN, 87.0% SPE, 0.921 AUC	[75]
2020	B-mode and TE	LightGBM	≥F2: 82% ACC, 75% SEN, 88% SPE, 0.87 AUC =F4: 88% ACC, 72% SEN, 90% SPE, 0.90 AUC	[76]
2020	B-mode	VGG	≥F2: 86.5% ACC, 91.3% SEN, 82.4% SPE, 0.866 AUC =F4: 88.3% ACC, 77.8% SEN, 93.7% SPE, 0.857 AUC	[77]
2020	SWE	SVM	pSWE: 0.96 AUC, 2D-SWE: 0.99 AUC	[78]
2020	B-mode	GoogLeNet	=F4: 91% ACC, 0.992 AUC	[79]
2020	SWE	CNN	≥F2: 0.94 AUC	[80]
2019	SWE	CNN	≥F2: 0.85 AUC; ≥F3: 0.98 AUC; =F4: 0.97 AUC	[81]
2019	B-mode and RF signals and CEUS	AdaBoost/SVM	0.85 AUC	[82]
2019	SWE	GoogLeNet	≥F1: 91% ACC, 0.97 AUC ≥F2: 92.5% ACC, 0.97 AUC ≥F3: 92.5% ACC, 0.96 AUC =F4: 95.5% ACC, 0.97 AUC	[83]
2019	RF signals	CNN	≥F2: 76.64% SEN, 71.72% SPE, 0.850 AUC ≥F3: 81.92% SEN, 89.74% SPE, 0.948 AUC =F4: 40.00% SEN, 94.79% SPE, 0.934 AUC	[84]
2018	B-mode	PNN	91.46% ACC, 92.16% SEN, 88.92% SPE	[85]
2017	B-mode	ResNet	Normal: 100%; Mild: 100%; Moderate: 90.91%; Severe: 93.33%	[86]
2017	B-mode	VGG + FCNet	96.06% ACC	[87]
2017	B-mode	CNN + SVM	0.869 ACC, 0.951 AUC	[88]
2017	TE and SWE	SVM	≥F2: 90.68% ACC, 91.02% SEN, 87.58% SPE, 93.37% AUC =F4: 93.52% ACC, 94.82% SEN, 90.41% SPE, 98.47% AUC	[89]
2017	Doppler and TE	ANN	88.9% SEN, 100.0% SPE, 0.990 AUC	[90]

Abbreviations: ACC, accuracy; AdaBoost, adaptive boosting; ANN, artificial neural network; AUC, area under the curve; CNN, convolutional neural network; MAE, mean absolute error; MLNN, multilayer neural network; MLP, Multilayer Perceptron; PRE, precision; LightGBM, light gradient boosting machine; SVM, support vector machine; PNN, probabilistic neural network; RMSE, root mean square error; SEN, sensitivity; SPE, specificity.

and significant fibrosis (≥F2) with AUC values of 0.96 for pSWE images and 0.99 for 2D-SWE images [78].

Previous work has also explored other types of data for diagnosing fibrosis, such as CDFI and RF data, or clinical data, such as platelet count, AST, and ALT levels. Li et al. proposed a deep learning method that relies on the M-mode RF data acquired in TE. Compared with LSM data obtained from TE, their approach produced better diagnosis of advanced fibrosis and cirrhosis [91]. Alempijevic et al. tested the performance of a model that only relied on Doppler parameters for predicting significant liver fibrosis with sensitivity and specificity values of 75.0% and 60.0%, respectively. When combining Doppler parameters with TE, age, platelet count, AST, and ALT levels, those values increased to 88.9% and 100%, respectively [90]. Liu et al. developed a CNN that integrated information from B-mode images of liver parenchyma with LSM and clinical parameters of individual patients. When this approach was used to diagnose significant fibrosis in chronic hepatitis B patients, it achieved significantly higher AUC (0.901) than corresponding values from competing methods (0.774–0.877) [67]. Brausch et al. deployed various machine learning algorithms for the non-invasive diagnosis of liver steatosis in NAFLD patients using one-dimensional RF signals. They achieved the highest average F1 score of 80.9% with an SVM model performing on wavelet transformed RF signals [72].

3.2. Diagnosis of focal liver diseases

Focal liver diseases are generally divided into benign and malignant lesions. Distinguishing between benign and malignant lesions is a necessary prerequisite for subsequent diagnosis and treatment of the disease. Further identification of specific diseases is the final target of diagnosis. Common benign lesions include cyst, liver abscess, echinococcosis, HEM, focal nodular hyperplasia (FNH), and hepatocellular adenoma (HCA). Typical malignant lesions include hepatocellular carcinoma (HCC), cholangiocarcinoma, combined HCC-cholangiocarcinoma, and metastatic hepatic carcinoma (MHC). Different cystic lesions, such as cyst, liver abscess, and echinococcosis, present strong similarities. FNH, HEM, HCC, MHC, and HCA also show strong similarities at the level of US images. AI technologies can be of great benefit in this application as they are proficient in analyzing image features and detecting minor differences.

Many researchers have devoted their efforts to the development of AI-assisted diagnosis of focal liver diseases, and they have obtained promising results (Table 3). Most studies have used only B-mode images as training data. Yamakawa et al. developed a CAD system based on VGG-19 to classify liver tumors into cyst, HEM, HCC, and MHC by utilizing approximately 71,000 US images of liver tumor. They achieved an

Table 3
Classification of focal liver diseases via US imaging and AI.

Year	Data type	Method	Best performance	Ref.
2022	B-mode	Detection transformer	Lesion detection: 90% SPE, 97% SEN Benign/malignant: 80% ACC, 81% SPE, 82% SEN	[92]
2022	CEUS	LR/SVM/RDF/KNN	Soft voting: 0.78 ACC, 0.76 SEN, 0.92 SPE, 0.84 AUC	[93]
2022	B-mode	Xception	HCC/FNH: 86.41% ACC, 96.08% SEN, 76.92% SPE, 87.50% F1 score	[94]
2022	CEUS	3D-CNN + SVM	Atypical HCC/FNH: 98.33% ACC, 98.06% SEN, 98.59% SPE	[95]
2022	B-mode	VGG	HCC/other: 93.4% ACC, 67.5% SEN, 96.0% SPE LM/other: 95.1% ACC, 62.8% SEN, 97.5% SPE HEM/other: 94.6% ACC, 91.0% SEN, 96.5% SPE cyst/other: 99.0% ACC, 99.0% SEN, 98.8% SPE	[96]
2021	B-mode	ResNet-18	HCC/other: 78.6% SEN, 82.6% SPE, 0.81 AUC	[97]
2021	B-mode	ResNet-50	Benign/malignant: 0.84 ACC, 0.87 SEN, 0.78 SPE, 0.86 AUC	[98]
2021	B-mode and SWE	SVM	Benign/malignant: 92.59% SEN, 87.5% SPE, 0.94 AUC	[99]
2021	B-mode	ResNet-50	Cyst/HCC/HEM/FFS/FFI: 95.3% ACC, 84.9% SEN, 97.1% SPE	[100]
2021	B-mode	VGG-16	Benign/malignant: 90.4% ACC, 95.0% SEN, 86.0% SPE, 0.970 AUC Cyst/HEM/LM/HCC: 82.2% ACC, 86.7% SEN, 89.7% SPE, 0.947 AUC	[101]
2021	B-mode	SVM	HCC/ICC: 87.18% ACC, 88.87% SEN, 86.67% SPE, 0.874 AUC	[102]
2021	B-mode	VGG-19	Benign/malignant: 94.3% ACC, 82.8% SEN, 96.7% SPE Cyst/HEM/HCC/LM: 91.1% ACC	[103]
2021	B-mode and CEUS	DenseNet + ResNet	HCC/normal: 98.20% ACC, 98.16% SEN, 98.24% SPE, 0.982 AUC	[104]
2021	B-mode	ResNet-50 v2	Benign/malignant: 100% SEN, 80% SPE, 0.904 AUC	[105]
2021	CEUS	SVM	Atypical HCC/FNH: 93.5% SEN, 84.9% SPE, 0.93 AUC	[106]
2021	CEUS	ResNet-152	Benign/malignant: 91.0% ACC, 92.7% SEN, 85.1% SPE, 0.934 AUC	[107]
2021	SWE	Random Forest	Benign/malignant: 0.908 ACC, 0.933 SEN, 0.850 SPE, 0.926 AUC	[108]
2021	CEUS	ResNet-50	FNH/HCC/HEM/HYPERM/HYPOM: 88% ACC	[109]
2020	B-mode	ResNet-18	Diagnosis of different tumor size: 1.1–2.0 cm: 0.941 ACC, 1.000 SEN, 0.500 SPE, 0.926 AUC 2.1–5.0 cm: 0.861 ACC, 0.891 SEN, 0.757 SPE, 0.899 AUC >5.0 cm: 0.835 ACC, 0.795 SEN, 0.939 SPE, 0.962 AUC	[110]
2020	CEUS	CNN	FNH/HCC/HEM/HYPERM/HYPOM: 95.71%	[111]
2020	B-mode	Radiomic analysis	HCC/non-HCC: 0.775 AUC	[112]
2020	B-mode	YOLO v3 + VGG-16	HCC/LM/HEM/Cyst/other: 91.1% SEN, 77.4% PRE, 0.837 F1-Score	[113]
2020	B-mode	VGG-19 + SVM	FLD/not: 98.40% ACC, 98.67% SEN, 98.12% SPE	[114]
2020	CEUS	Naive Bayes	FNH/I-HCA: 95.9% ACC, 93.4% SEN, 97.6% SPE, 0.97 AUC	[115]
2020	B-mode	CNN	HCC/PAR: 91% ACC, 94.37% SEN, 88.38% SPE, 95% AUC	[116]
2019	B-mode	VGG	Benign/malignant: 94.8% ACC, 93.8% SEN, 95.2% SPE Cyst/HEM/HCC/LM: 88.0% ACC	[117]
2019	B-mode	ResNet-50/DenseNet-121	FLL/not: 0.935 AUC malignant/benign: 0.942 AUC HEM/LM/HCC/Cyst/FNH: 0.916 AUC	[118]
2019	CEUS	CNN	HCC/FNH: 93.1% ACC, 94.5% SEN, 93.6% SPE, 0.97 AUC	[119]
2018	B-mode	CNN	HCC/PAR: 81.70% ACC, 78.66% SEN, 84.76% SPE, 0.88 AUC HCC/HEM: 78.03% ACC, 63.62% SEN, 92.46% SPE, 0.90 AUC	[120]
2018	B-mode	SVM	HCC/PAR: 68.75% ACC, 68.8% AUC	[121]
2018	B-mode and SWE and SWV	SVM	Benign/malignant: 0.94 AUC HCC/other tumor: 0.97 AUC	[122]
2018	B-mode and CEUS	SVM	Benign/malignant: 81.1% ACC, 90.0% SEN, 71.1% SPE, 0.883 AUC	[123]
2018	CEUS	DCCA-MKL	Benign/malignant: 90.41% ACC, 93.56% SEN, 86.89% SPE, 0.953 AUC, 79.44% Youden Index	[124]
2017	B-mode	PNN	Normal/benign/malignant: 92.95% ACC, 90.80% SEN, 97.44% SPE, 0.941 AUC	[125]
2017	CEUS	SVM	Benign/malignant: 91.8% ACC, 94.0% SEN, 87.1% SPE	[126]
2017	B-mode	Auto-encoder	Cyst/HEM/HCC/normal: 97.2% ACC, 98.0% SEN, 95.7% SPE	[127]

Abbreviations: AUC, area under the curve; ACC, accuracy; CNN, convolutional neural network; DCCA, deep canonical correlation analysis; FFI, focal fatty infiltration; FFS, focal fatty sparing; FNH, focal nodular hyperplasia; HCC, hepatocellular carcinoma; HEM, hemangioma; HYPERM, hypervascular metastases; HYPOM, hypovascular metastases; I-HCA, inflammatory hepatocellular adenoma; KNN, k-nearest neighbor; LM, liver metastasis; LR, logistic regression; MKL, multiple kernel learning; PAR, cirrhotic parenchyma; PNN, probabilistic neural network; PRE, precision; RDF: random forest; SEN, sensitivity; SPE, specificity; SVM, support vector machine.

accuracy of 91.1% for four-class classification, and 94.3% for the benign/malignant classification [103]. Nishida et al. constructed three AI models using small, middle, and large US image datasets which yield diagnostic accuracies of 86.8%, 91.0%, and 91.1%, respectively, for four types of tumors, and 91.3%, 94.3%, and 94.3% for malignant tumor. These values are higher than those produced by human experts [96]. Using a fine-tuned CNN pre-trained on ImageNet with ResNet-50 architecture to differentiate between benign and malignant lesions, Xi et al. achieved higher test accuracy than expert radiologists [98]. Tiyarattanachai et al. developed a CNN that was able to detect focal liver lesions with 75.0% accuracy, 84.9% sensitivity, and 97.1% specificity. Their model was also able to diagnose HCC with 81.5% accuracy, 94.4% sensitivity, and 97.4% specificity [100]. Mostafiz et al. presented a machine vision approach to detect focal liver lesions with a pre-trained CNN model that fused features extracted using Gabor wavelet transform and local binary patterns. These authors achieved an accuracy of 98.4% [114].

Some researchers have adopted a two-stage strategy whereby the classification task is broken down into two steps: (1) detection and segmentation of abnormalities, followed by (2) classification of the resulting patches. Separate implementation with two models may facilitate learning of the ensemble model. Ryu et al. developed a CNN system that jointly segmented and classified hepatic lesions. This architecture achieved higher accuracy (82.2%) than the classification-only system (79.8%) when classifying four types of hepatic lesions [101]. Schmauch et al. used a supervised attention mechanism to detect and characterize focal liver lesions. Their ensemble model reached mean AUC scores of 0.935, 0.942, and 0.916 for lesion detection, malignancy diagnosis, and lesion characterization, respectively [118]. Nakashima et al. proposed a liver detection method using YOLO v3 to find candidate regions, and

Table 4
US-guided hepatic surgery.

Year	Classification	Method	Application	Result	Ref.
2021	Segmentation	VGG-16	Hepatic lesion segmentation	The JI of 68.5%	[132]
2022	Segmentation	U-Net	Segment CEUS and identify the lesions of liver	IoU = 0.7, recall = 0.76 and precision = 0.86	[133]
2018	Segmentation	CNN	Hepatic vasculature segmentation	A mean region IoU of 0.696	[134]
2019	Segmentation	FCNN	Segment the blood region from the US images	Yield better performance than the existing approaches	[135]
2019	Segmentation	2D U-Net	Segment the vessels and liver borders from US images	The mean Dice scores of 0.5 for vessel structures and mean Dice scores of 0.6 for liver boundary	[136]
2020	Segmentation	3D U-Net	Hepatic vessel segmentation from the 3D US volumes	The Dice scores of 0.77, 0.65 and 0.66 achieved for all vasculature, hepatic vein and portal vein, respectively	[137]
2021	Segmentation	2D U-Net	Segment multiple liver vessel instances in 2D LUS images	The mean Dice scores range from 0.543 to 0.706	[138]
2020	Registration	3D U-Net	2D-US to 3D-CT/MR registration	The angle and distance errors of 12.7 ± 6.2° and 4.9 ± 3.1 mm	[139]
2021	Registration	3D U-Net	2D-US to 3D-CT/MR registration	The average registration errors of 11.6 and 4.7 mm	[140]
2021	Registration	CBIR	LUS images to the preoperative CT registration	The registration accuracy ranges from 5.7 to 16.4 mm with a success rate of 78%	[142]
2019	Motion monitoring	PCA and SFA	Intra-fraction respiratory motion tracking	The mean tracking error of 1.14 ± 1.16 mm, the tracking time of 15 ms per frame	[143]
2017	Motion monitoring	Block matching	The real-time 2D ultrasound tracking of liver vessels	The mean tracking error of 0.72 ± 1.25 mm, and the image processing speed per landmark between 73 and 234 FPS after training set accumulation	[144]
2017	Motion monitoring	Supporters	Motion tracking in liver from 2D US images	1.04 mm mean and 2.26 mm 95%ile tracking error for all targets	[145]
2019	Motion monitoring	VGG-16	Estimate six-axis liver movement amount from 2D US images	Show the effectiveness of the movement amount perpendicular to the US image	[146]
2020	Motion monitoring	BCDU-Net	Estimate 3D liver motion from 2D US images	The mean absolute error of 0.0645 mm/frame for the out-of-plane direction	[147]
2021	Robot ultrasound	RL	Robot-assisted US imaging	Realize real-time US probe controlling, soft surface constant force tracking, and automatic imaging	[148]

Abbreviations: 2D, two-dimensional; 3D, three-dimensional; BCDU-Net, bi-directional convolutional LSTM U-Net with densely connected convolutions; CBIR, content-based image retrieval; CEUS, contrast-enhanced ultrasound; CNN, convolutional neural network; FCNN, fully convolutional neural network; FPS, frames per second; IoU, intersection over union; JI, mean Jaccard index; LUS, laparoscopic ultrasound; PCA, principal component analysis; RL, reinforcement learning; SFA, slow feature analysis.

VGG-16 to classify lesions into HCC, MHC, HEM, cyst, and tumor not belonging to any of those categories. Their approach produced a mean F-measure of 0.837 for overall tumor detection [113].

As an important diagnostic tool for liver cancer, CEUS was also involved in research on AI-based diagnosis. Mitrea et al. assessed the possibility of obtaining automatic diagnoses for HCC from B-mode and CEUS images using various CNN classifiers and achieved accuracy above 97% with a multimodal combined classifier [104]. Li et al. investigated the feasibility of exploiting ultrasonic signatures derived from CEUS images for improving performance in differentiating between FNH and atypical HCC. By combining ultrasonics features with scores produced by expert radiologists, they achieved a significantly higher AUC (0.93) than those associated with expert scores or ultrasonics features alone [106]. Hu et al. developed an AI-assisted strategy to improve the identification of malignant versus benign focal liver lesions using CEUS. With the assistance of AI, radiologists exhibited a significant improvement in sensitivity (from 88.4%–90.2% to 97.0%–99.4%) and accuracy (from 82.0%–86.7% to 91.0%–92.9%) [107]. Denis et al. designed a computer tool to distinguish between FNH and inflammatory HCA using qualitative or quantitative CEUS data. They obtained accuracy values of 93.6% and 95.9% with qualitative parameters and quantitative parameters, respectively [115]. Pan et al. developed a CAD system for classifying liver lesions from CEUS video data analyzed by three-dimensional (3D)-CNN operators and achieved an average accuracy of 93.1% [119].

The combination of multimodal US data and clinical data deserves much interest, but there are only a few relevant studies. Zhou et al. built a predictive model on top of a CNN architecture that relies on clinical features for differentiating between HCC and other malignancies. With an AUC value of 0.81, their model outperformed the CNN on its own [97]. Yao et al. established a radiomics analysis system for the differentiation between malignant and benign lesions, for diagnosis of HCC, and for prognostic prediction. Their system relied on multimodal US data including B-mode, SWE, and shear wave viscosity imaging. They also included three biomarkers for comparison [122]. Wang et al. used 2D-SWE-based ultrasonics to differentiate between malignant and benign lesions. Their combined score (SWE measurements and ultrasonics features extracted from 2D-SWE images) showed the best performance with 92.6% sensitivity, 87.5% specificity, and 0.94 AUC [99].

3.3. US-guided hepatic surgery

3.3.1. US image segmentation

US images pose serious challenges for automatic segmentation because they are characterized by acoustic shadows, poor contrast, and presence of spots [128]. Missing and incomplete structural boundaries further increase the difficulty of segmentation. Most traditional US segmentation methods are not fully automated, including intensity gradient, level set, active contour, and other model-based methods [129]. Automatic segmentation methods based on various types of neural networks are active areas of current research [130].

Conventional applications of segmentation algorithms are typically used to delineate organs and lesions in the liver. In the case of organs, specific liver organs including the hepatic vasculature can be segmented from the US images for further analysis. In the case of lesions such as liver tumors, their segmentation can facilitate subsequent disease classification and diagnosis. Clinicians typically use manual or semi-automatic methods to identify lesion structures located in the liver. These procedures are time-consuming and costly. Considering the many low-contrast objects that are present in noisy and complex US images, Xu et al. proposed an adaptive method for setting contrast level that combines global statistics and boundary statistics for liver tumor segmentation in minimally invasive surgery [131]. Ryu et al. developed a CNN system to

segment hepatic lesions from US images. They adapted a semiautomatic segmentation method based on the VGG-16 network with batch normalization. The performance of hepatic lesion segmentation was evaluated based on the Jaccard index, and the mean Jaccard index was 68.5% [132]. Using a version of U-Net, Mamuleanu et al. segmented CEUS images and identified lesions in the liver with an intersection over union value of 0.7, a recall value of 0.76, and precision equal to 0.86 [133] (see Table 4).

In addition to lesion segmentation in the liver, several deep learning methods have been developed for the segmentation of hepatic vasculature. A pipelined network including a CNN was trained to position vascular regions and then segment the vessel in liver US images via an unsupervised clustering method, achieving a mean intersection over union of 0.696 [134]. An improved fully convolutional neural network was developed to automatically segment blood regions from US images. Deep supervision of the network improved learning of US image characteristics and yielded better performance than competing approaches [135]. Moreover, a 2D U-Net framework was used to segment vessels and liver borders from US images [136]. A reduced 3D U-Net was also used for hepatic vessel segmentation from 3D US volumes acquired during surgery [137]. When segmenting vessel structures, mean Dice scores were 0.5 for 2D U-Net and 0.7 for 3D U-Net. The segmentation results detailed above were then used as regions of interest to improve registration procedures and obtain sufficient target registration accuracy. A 2D U-Net was also used to segment multiple liver vessel instances from 2D laparoscopic US (LUS) images, with mean Dice scores ranging between 0.543 and 0.706. The LUS-CT registration pipeline was then automatically initialized without a tracking device [138].

3.3.2. *Multimodal image registration*

US imaging carries the advantages of real-time implementation, nonionized radiation, and low cost. At the same time, this technology is hampered by poor image quality and low soft tissue contrast. These drawbacks can be compensated via registration and fusion with preoperative CT/MR images. However, the task of image registration is made challenging by respiratory movements and differences in imaging modes. Recently, the focus of registration techniques has shifted to methods based on deep learning.

In addition to registration methods based on segmentation of hepatic vasculature [136–138], there are also studies based on pose estimation to realize fully automatic 2D US to 3D CT/MR registration. Wei et al. proposed a deep learning network pipeline consisting of a classification network and a segmentation network to detect the US plane in CT/MR volumes, and then achieved rigid registration through plane regression [139]. This work was further extended and a novel pipeline was proposed to improve registration accuracy. In place of the regression procedure, plane estimation was achieved by a 3D U-Net architecture with dual-channel input. After determining the US angle, the position of the US plane in the 3D CT/MR was estimated through segmentation [140].

LUS is an imaging tool that can improve the safety of surgical processes by imaging deep structures, such as blood vessels and tumors [141]. However, LUS has limited field of view and requires the expert skills of surgeons to correctly interpret the resulting images. In addition, some tumors are iso-echoic and difficult to visualize in LUS images. It has, therefore, been proposed to realize image guidance via registration of LUS images with preoperative CT images. A registration method based on content-based image retrieval was proposed to eliminate the requirements of tracking or manual initialization [142]. Using a series of five untracked images, the results showed a registration accuracy ranging between 5.7 mm and 16.4 mm, with a success rate of 78%.

3.3.3. *Other applications*

Some studies used machine learning methods to achieve motion monitoring in abdominal radiotherapy. An abdominal motion tracking method based on anatomical features was proposed [143]. The specific motion patterns of individual patients were extracted via principal component analysis and slow feature analysis. This method significantly reduced the processing time for tracking respiratory movement. Shepard et al. also proposed a 2D algorithm for real-time tracking of US features to help radiotherapy motion management [144]. The proposed algorithm utilized a block matching algorithm based on similarity measurements, combined with training methods and multiple simultaneous templates for real-time 2D US tracking of liver vessels. The initial experiment showed that its accuracy was equivalent to, or higher than, the accuracy achieved by competing 2D tracking methods. Furthermore, its calculation speed was sufficiently high to meet the requirements of real-time application in the radiotherapy environment. In US imaging, acoustic shadows and other artifacts may reduce target visibility, resulting in large tracking errors. To minimize these errors, a method based on a computer vision tracking technology was proposed. This method relied on surrounding motion information to improve the robustness of motion tracking on the 2D image sequence recorded from the liver [145]. When entered into the challenge associated with the Liver Ultrasound Tracking (CLUST)-2015 dataset, it delivered a state-of-the-art real-time tracking solution by using optic flow and elliptic vessel models.

Deep learning in combination with 2D US imaging was also used to estimate 3D liver motion, with the goal of tracking the location of liver tumors during treatment [146,147]. The relative motion between the liver and the US probe was estimated by CNNs to achieve six-axis movement estimation of the liver. Processing speed was improved by using multitask learning. In experiments with liver phantoms, organ motion was tracked precisely and robustly by using the proposed method. The accuracy of movement estimation was further improved by using a modified LSTM U-Net, which led to a mean absolute error of 0.0645 mm/frame for the out-of-plane direction.

To overcome the shortcomings associated with manual positioning of the US probe guided by user experience, robot-assisted US imaging is used for stable and long-term imaging of moving organs. Ning et al. developed an autonomous robot US imaging system based on reinforcement learning to control US probe positioning in real-time, track soft surface constant force, and perform automatic imaging [148]. Experiments showed that this method was stable and feasible to control the US probe autonomously and accurately.

4. Discussion

With pressing demands for clinical applications and the development of new technologies, US imaging offers a variety of imaging modes: B-mode imaging, Doppler imaging, CEUS, and QUS, all of which can be used in the liver. B-mode US imaging is mainly used to image the anatomical structure of the liver. US elastography technologies such as TE, pSWE, and 2D-SWE are used to assess the stiffness or elasticity of the liver. Doppler imaging is commonly used to assess hepatic blood flow. CEUS is used to improve the detection of hepatic blood vessels and tumors. QUS is important for the quantification of hepatic steatosis.

At present, the rapid development of AI technologies makes the various modes of US imaging more flexible and capable. AI methods based on US images have been widely used in the diagnosis and treatment of hepatic diseases, and have achieved encouraging results. Recent studies have demonstrated the potential of AI-assisted US imaging in grading steatosis, staging of fibrosis, detection of focal liver lesions, US image segmentation, multimodal image registration, and US-guided surgery.

Compared with other medical imaging modes, the quality of US images highly depends on the operator and is also directly affected by examination conditions. These factors have hindered the application of deep learning technologies in the field of US-based diagnosis. However, the use of AI-based US imaging technologies may reduce the dependence on operators, and make US-guided diagnosis and treatment more intelligent. This synergy between humans and US systems will not only help decision-making, but also improve the clinical workflow of US imaging and reduce medical costs. Hence, this approach carries enough potential

to have a transformational effect on US-aided diagnosis of hepatic diseases.

The success of deep learning methods depends on big data. To achieve accurate US-guided diagnosis for hepatic diseases, a larger and more balanced dataset is required. However, most US-based deep learning applications are trained and evaluated on limited datasets obtained from a single medical center and a single US system. To overcome the problem of limited datasets, we can use the transfer learning method to train deep learning models and fine-tune them on new datasets obtained from different medical centers and/or different US systems. In addition, data enhancement technology can also be used to expand the available datasets. A similar goal may be achieved by generating composite images from generative adversarial network to improve the generalization ability of deep learning models [98,149]. In addition, the current deep learning models for US-based diagnosis mainly use 2D US images for prediction. However, the information of 2D images is limited and cannot fully represent the nature of liver lesions. A deep learning model trained on 3D US data, such as US movie clips with multiple views of the lesion and spatiotemporal US data, can potentially improve diagnostic accuracy and develop a more complete account of lesion characteristics. In addition, it is possible to develop a deep learning model trained on multimodal images, such as B-mode, Doppler, contrast-enhanced, and SWE US images [75]. These multimodal images provide complementary information and can therefore improve the diagnostic accuracy of deep learning models. In addition, it is possible to construct AI diagnostic algorithms that integrate imaging features, clinical information, laboratory parameters, and pathological information to help clinicians make a personalized prediction based on all available data and provide personalized medical care. In the future, with the development of AI technology for registration, motion estimation, and robot control, AI-based US imaging will also play a more important role in intraoperative navigation for hepatic diseases.

5. Conclusion

With their rapid development, US imaging technologies have played an important role in the diagnosis and treatment of hepatic diseases. The integration and development of computer-aided US diagnosis technology with AI technology can help clinicians improve detection efficiency and classification of liver lesions. These technologies can aid effective clinical treatment of the liver and are able to predict the response of the liver after treatment. However, relatively poor imaging quality hinders the application of AI technology to US images. At present, the field of AI in US imaging is still in its early stages. In the future, with the progress of AI technology, AI-based US imaging will make important contributions in its application to hepatic diseases.

Funding

The authors acknowledge support from the National Natural Science Foundation of China (81901844, 82027807, 61871251) and the Beijing Municipal Natural Science Foundation (L192013, 7212202, M22018).

Author contributions

Longfei Ma, Rui Wang: Conceptualization, Investigation, Writing-Original Draft; Qiong He, Lijie Huang, Xinyue Wei: Investigation, Formal Analysis; Yanan Du: Investigation; Jianwen Luo: Supervision, Reviewing and Editing; Hongen Liao: Supervision, Funding Acquisition, Project Administration, Reviewing and Editing.

Acknowledgments

The authors thank the reviewers for their constructive suggestions.

Declaration of competing interest

The authors declare that they have no known competing financial interests or personal relationships that could have appeared to influence the work reported in this paper.

Data available statement

Not applicable.

Ethics statement

Not applicable.

Informed consent

None.

References

[1] Field KM, Dow C, Michael M. Part i: liver function in oncology: biochemistry and beyond. Lancet Oncol 2008;9:1092–101. https://doi.org/10.1016/s1470-2045(08)70279-1.
[2] Colombo M. Diagnosis of liver nodules within and outside screening programs. Ann Hepatol 2015;14:304–9. https://doi.org/10.1016/s1665-2681(19)31268-2.
[3] Zhou L, Wang J, Yu S, et al. Artificial intelligence in medical imaging of the liver. World J Gastroenterol 2019;25:672–82. https://doi.org/10.3748/wjg.v25.i6.672.
[4] Li YF, Wang XT, Zhang J, et al. Applications of artificial intelligence (ai) in researches on non-alcoholic fatty liver disease(nafld) : a systematic review. Rev Endocr Metab Disord 2022;23:387–400. https://doi.org/10.1007/s11154-021-09681-x.
[5] Janiesch C, Zschech P, Heinrich K. Machine learning and deep learning. Electron Mark 2021;31:685–95. https://doi.org/10.1007/s12525-021-00475-2.
[6] Xiang K, Jiang B, Shang D. The overview of the deep learning integrated into the medical imaging of liver: a review. Hepatol Int 2021;15:868–80. https://doi.org/10.1007/s12072-021-10229-z.
[7] Khan R, Luo Y, Wu F. Machine learning based liver disease diagnosis: a systematic review. Neurocomputing 2022;468:492–509. https://doi.org/10.1016/j.neucom.2021.08.138.
[8] Dong S, Wang P, Abbas K. A survey on deep learning and its applications. Comput Sci Rev 2021;40:22. https://doi.org/10.1016/j.cosrev.2021.100379.
[9] Litjens G, Kooi T, Bejnordi BE, et al. A survey on deep learning in medical image analysis. Med Image Anal 2017;42:60–88. https://doi.org/10.1016/j.media.2017.07.005.
[10] Wei JW, Jiang HY, Gu DS, et al. Radiomics in liver diseases: current progress and future opportunities. Liver Int 2020;40:2050–63. https://doi.org/10.1111/liv.14555.
[11] Hu WM, Yang HY, Xu HF, et al. Radiomics based on artificial intelligence in liver diseases: where are we? Gastroenterol Rep 2020;8:90–7. https://doi.org/10.1093/gastro/goaa011.
[12] Smith SE, Salanitri J, Lisle D. Ultrasound evaluation of soft tissue masses and fluid collections. Semin Muscoskel Radiol 2007;11:174–91. https://doi.org/10.1055/s-2007-1001882.
[13] Chami L, Lassau N, Chebil M, et al. Imaging of melanoma: usefulness of ultrasonography before and after contrast injection for diagnosis and early evaluation of treatment. Clin Cosmet Invest Dermatol 2011;4:1–6. https://doi.org/10.2147/ccid.S13499.
[14] Fenster A, Downey DB. Three-dimensional ultrasound imaging and its use in quantifying organ and pathology volumes. Anal Bioanal Chem 2003;377:982–9. https://doi.org/10.1007/s00216-003-2169-6.
[15] Nyland TG, Hager DA. Sonography of the liver, gallbladder, and spleen. Vet Clin N Am Small Anim Pract 1985;15:1123–48. https://doi.org/10.1016/s0195-5616(85)50361-7.
[16] Castellano G, Bonilha L, Li LM, et al. Texture analysis of medical images. Clin Radiol 2004;59:1061–9. https://doi.org/10.1016/j.crad.2004.07.008.
[17] Dreher C, Linde P, Boda-Heggemann J, et al. Radiomics for liver tumours. Strahlenther Onkol 2020;196:888–99. https://doi.org/10.1007/s00066-020-01615-x.
[18] Jansson T, Persson HW, Lindstrom K. Estimation of blood perfusion using ultrasound. Proc Inst Mech Eng Part H J Eng Med 1999;213:91–106. https://doi.org/10.1243/0954411991534834.
[19] McNaughton DA, Abu-Yousef MM. Doppler us of the liver made simple. Radiographics 2011;31:161–U233. https://doi.org/10.1148/rg.311105093.
[20] Go S, Kamaya A, Jeffrey B, et al. Duplex Doppler ultrasound of the hepatic artery a window to diagnosis of diffuse liver pathology. Ultrasound Q 2016;32:58–66. https://doi.org/10.1097/ruq.0000000000000166.
[21] Quaia E. Microbubble ultrasound contrast agents: an update. Eur Radiol 2007;17:1995–2008. https://doi.org/10.1007/s00330-007-0623-0.

[22] Lu K, Jiang Y-x. Ultrasound contrast agents in liver imaging. Zhongguo yi xue ke xue yuan xue bao. Acta Acad Med Sin 2002;24:519–22.
[23] Claudon M, Dietrich CF, Choi BI, et al. Guidelines and good clinical practice recommendations for contrast enhanced ultrasound (ceus) in the liver - update 2012 a wfumb-efsumb initiative in cooperation with representatives of afsumb, aium, asum, flaus and icus. Ultrasound Med Biol 2013;39:187–210. https://doi.org/10.1016/j.ultrasmedbio.2012.09.002.
[24] Dietrich CF, Nolsoe CP, Barr RG, et al. Guidelines and good clinical practice recommendations for contrast enhanced ultrasound (ceus) in the liver - update 2020 wfumb in cooperation with efsumb, afsumb, aium, and flaus. Ultraschall der Med 2020;41:562–85. https://doi.org/10.1055/a-1177-0530.
[25] Li C, Liu Y, Xu JY, et al. Contrast-enhanced intraoperative ultrasonography with kupffer phase may change treatment strategy of metastatic liver tumors - a single-centre prospective study. Therapeut Clin Risk Manag 2021;17:789–96. https://doi.org/10.2147/tcrm.S317469.
[26] Sigrist RMS, Liau J, El Kaffas A, et al. Ultrasound elastography: review of techniques and clinical applications. Theranostics 2017;7:1303–29. https://doi.org/10.7150/thno.18650.
[27] Bamber J, Cosgrove D, Dietrich CF, et al. Efsumb guidelines and recommendations on the clinical use of ultrasound elastography. Part 1: basic principles and technology. Ultraschall der Med 2013;34:169–84. https://doi.org/10.1055/s-0033-1335205.
[28] Gennisson JL, Deffieux T, Fink M, et al. Ultrasound elastography: principles and techniques. Diag Intervent Imag 2013;94:487–95. https://doi.org/10.1016/j.diii.2013.01.022.
[29] Sandrin L, Fourquet B, Hasquenoph JM, et al. Transient elastography: a new noninvasive method for assessment of hepatic fibrosis. Ultrasound Med Biol 2003;29:1705–13. https://doi.org/10.1016/j.ultrasmedbio.2003.07.001.
[30] Ferraioli G, Tinelli C, Lissandrin R, et al. Point shear wave elastography method for assessing liver stiffness. World J Gastroenterol 2014;20:4787–96. https://doi.org/10.3748/wjg.v20.i16.4787.
[31] Bercoff J, Tanter M, Fink M. Supersonic shear imaging: a new technique for soft tissue elasticity mapping. IEEE Trans Ultrason Ferroelectrics Freq Control 2004;51:396–409. https://doi.org/10.1109/tuffc.2004.1295425.
[32] Song PF, Zhao H, Manduca A, et al. Comb-push ultrasound shear elastography (cuse): a novel method for two-dimensional shear elasticity imaging of soft tissues. IEEE Trans Med Imag 2012;31:1821–32. https://doi.org/10.1109/tmi.2012.2205586.
[33] Chinese Society of Hepatology CMA, Chinese Society of Gastroenterology CMA, Chinese Society of Infectious Diseases CMA. Consensus on the diagnosis and therapy of hepatic fibrosis in 2019. Chin J Hepatol 2019;27:657–67. https://doi.org/10.1073/pnas.80.20.6332.
[34] Dietrich CF, Bamber J, Berzigotti A, et al. Efsumb guidelines and recommendations on the clinical use of liver ultrasound elastography, update 2017 (long version). Ultraschall der Med 2017;38:E16–47. https://doi.org/10.1055/s-0043-103952.
[35] Paige JS, Bernstein GS, Heba E, et al. A pilot comparative study of quantitative ultrasound, conventional ultrasound, and mri for predicting histology-determined steatosis grade in adult nonalcoholic fatty liver disease. Am J Roentgenol 2017;208:W168–77. https://doi.org/10.2214/ajr.16.16726.
[36] Lin SC, Heba E, Wolfson T, et al. Noninvasive diagnosis of nonalcoholic fatty liver disease and quantification of liver fat using a new quantitative ultrasound technique. Clin Gastroenterol Hepatol 2015;13:1337. https://doi.org/10.1016/j.cgh.2014.11.027.
[37] Nguyen TN, Podkowa AS, Tam AY, et al. Characterizing fatty liver in vivo in rabbits, using quantitative ultrasound. Ultrasound Med Biol 2019;45:2049–62. https://doi.org/10.1016/j.ultrasmedbio.2019.03.021.
[38] Sasso M, Beaugrand M, de Ledinghen V, et al. Controlled attenuation parameter (cap): a novel vcte (tm) guided ultrasonic attenuation measurement for the evaluation of hepatic steatosis: preliminary study and validation in a cohort of patients with chronic liver disease from various causes. Ultrasound Med Biol 2010;36:1825–35. https://doi.org/10.1016/j.ultrasmedbio.2010.07.005.
[39] Liu Q, Liu Z, Xu W, et al. Diagnosis of significant liver fibrosis by using a dcnn model with fusion of features from us b-mode image and nakagami parametric map: an animal study. IEEE Access 2021;9:89300–10. https://doi.org/10.1109/ACCESS.2021.3064879.
[40] Sanabria S, Dahl J, Pirmoazen A, et al. Learning steatosis staging with two-dimensional convolutional neural networks: comparison of accuracy of clinical b-mode with a co-registered spectrogram representation of rf data. In: Proceedings of the 2020 IEEE International Ultrasonics Symposium (IUS); 2020. p. 1–4. https://doi.org/10.1109/IUS46767.2020.9251329.
[41] Paik JM, Golabi P, Younossi Y, et al. Changes in the global burden of chronic liver diseases from 2012 to 2017: the growing impact of nafld. Hepatology 2020;72:1605–16. https://doi.org/10.1002/hep.31173.
[42] Sanabria SJ, Pirmoazen AM, Dahl J, et al. Comparative study of raw ultrasound data representations in deep learning to classify hepatic steatosis. Ultrasound Med Biol 2022;48:2060–78. https://doi.org/10.1016/j.ultrasmedbio.2022.05.031.
[43] Li B, Tai D-I, Yan K, et al. Accurate and generalizable quantitative scoring of liver steatosis from ultrasound images via scalable deep learning. World J Gastroenterol 2022;28:2494–508. https://doi.org/10.3748/wjg.v28.i22.2494.
[44] Byra M, Han A, Boehringer A, et al. Liver fat assessment in multiview sonography using transfer learning with convolutional neural networks. J Ultrasound Med 2022;41:175–84. https://doi.org/10.1002/jum.15693.
[45] Rhyou S, Yoo J. Cascaded deep learning neural network for automated liver steatosis diagnosis using ultrasound images. Sensors 2021;21. https://doi.org/10.3390/s21165304.
[46] Das A, Connell M, Khetarpal S. Digital image analysis of ultrasound images using machine learning to diagnose pediatric nonalcoholic fatty liver disease. Clin Imag 2021;77:62–8. https://doi.org/10.1016/j.clinimag.2021.02.038.
[47] Constantinescu E, Udristoiu A, Udristoiu S, et al. Transfer learning with pre-trained deep convolutional neural networks for the automatic assessment of liver steatosis in ultrasound images. Med Ultrasonogr 2021;23:135–9. https://doi.org/10.11152/mu-2746.
[48] Chou T, Yeh H, Chang C, et al. Deep learning for abdominal ultrasound: a computer-aided diagnostic system for the severity of fatty liver. J Chin Med Assoc 2021;84:842–50. https://doi.org/10.1097/JCMA.0000000000000585.
[49] Che H, Brown L, Foran D, et al. Liver disease classification from ultrasound using multi-scale cnn. Int J Comput Assist Radiol Surg 2021;16:1537–48. https://doi.org/10.1007/s11548-021-02414-0.
[50] Sanabria S, Dahl J, Pirmoazen A, et al. Multi-parametric ultrasound tissue characterization (mutc) as a surrogate to magnetic resonance imaging (mri) for non-alcoholic fatty liver disease (nafld) characterization. In: Proceedings of the 2020 IEEE International Ultrasonics Symposium (IUS); 2020. p. 1–4. https://doi.org/10.1109/IUS46767.2020.9251805.
[51] Han A, Byra M, Heba E, et al. Noninvasive diagnosis of nonalcoholic fatty liver disease and quantification of liver fat with radiofrequency ultrasound data using one-dimensional convolutional neural networks. Radiology 2020;295:342–50. https://doi.org/10.1148/radiol.2020191160.
[52] Chen J, Chao Y, Tsai Y, et al. Clinical value of information entropy compared with deep learning for ultrasound grading of hepatic steatosis. Entropy 2020;22. https://doi.org/10.3390/e22091006.
[53] Cao W, An X, Cong L, et al. Application of deep learning in quantitative analysis of 2-dimensional ultrasound imaging of nonalcoholic fatty liver disease. J Ultrasound Med 2020;39:51–9. https://doi.org/10.1002/jum.15070.
[54] Byra M, Styczynski G, Szmigielski C, et al. Adversarial attacks on deep learning models for fatty liver disease classification by modification of ultrasound image reconstruction method. In: Proceedings of the 2020 IEEE International Ultrasonics Symposium (IUS). IEEE; 2020. p. 1–4. https://doi.org/10.1109/IUS46767.2020.9251568.
[55] Reddy D, Rajalakshmi P. A novel web application framework for ubiquitous classification of fatty liver using ultrasound images. In: 2019 IEEE 5th World Forum on Internet of Things (Wf-Iot); 2019. p. 502–6. https://doi.org/10.1109/WF-IoT.2019.8767283.
[56] Neogi N, Adhikari A, Roy M. Use of a novel set of features based on texture anisotropy for identification of liver steatosis from ultrasound images: a simple method. Multimed Tool Appl 2019;78:11105–27. https://doi.org/10.1007/s11042-018-6675-0.
[57] Liu Z. Study on diagnosis of fatty liver based on ultrasonic rf signal. In: 2019 3rd International Conference on Imaging, Signal Processing and Communication (ICISPC); 2019. p. 117–20. https://doi.org/10.1109/ICISPC.2019.8935802.
[58] Chen C, Chen T, Lu N, et al. Classification for liver ultrasound tomography by posterior attenuation correction with a phantom study. Proc IME H J Eng Med 2019;233:1100–12. https://doi.org/10.1177/0954411919871123.
[59] Sharma V, Juglan KC. Automated classification of fatty and normal liver ultrasound images based on mutual information feature selection. IRBM 2018;39:313–23. https://doi.org/10.1016/j.irbm.2018.09.006.
[60] Salvati A, Di Lascio N, Avigo C, et al. Machine learning approaches for non-invasive ultrasound-based quantitative assessment of liver steatosis. Dig Liver Dis 2018;50:E225–6. https://doi.org/10.1016/S1590-8658(18)30630-3.
[61] Reddy D, Bharath R, Rajalakshmi P. A novel computer-aided diagnosis framework using deep learning for classification of fatty liver disease in ultrasound imaging. In: 2018 IEEE 20th International Conference on E-Health Networking, Applications and Services (Healthcom). IEEE; 2018. p. 1–5. https://doi.org/10.1109/HealthCom.2018.8531118.
[62] Reddy D, Bharath R, Rajalakshmi P. Classification of nonalcoholic fatty liver texture using convolution neural networks. In: 2018 IEEE 20th International Conference on E-Health Networking, Applications and Services (Healthcom); 2018. p. 1–4. https://doi.org/10.1109/HealthCom.2018.8531193.
[63] Byra M, Styczynski G, Szmigielski C, et al. Transfer learning with deep convolutional neural network for liver steatosis assessment in ultrasound images. Int J Comput Assist Radiol Surg 2018;13:1895–903. https://doi.org/10.1007/s11548-018-1843-2.
[64] Kuppili V, Biswas M, Sreekumar A, et al. Extreme learning machine framework for risk stratification of fatty liver disease using ultrasound tissue characterization. J Med Syst 2017;41:1–20. https://doi.org/10.1007/s10916-017-0797-1.
[65] Duan YY, Qin J, Qiu WQ, et al. Performance of a generative adversarial network using ultrasound images to stage liver fibrosis and predict cirrhosis based on a deep-learning radiomics nomogram. Clin Radiol 2022;77:e723–31. https://doi.org/10.1016/j.crad.2022.06.003.
[66] Zhou Z, Zhang Z, Gao A, et al. Liver fibrosis assessment using radiomics of ultrasound homodyned-k imaging based on the artificial neural network estimator. Ultrason Imag 2022;44:229–41. https://doi.org/10.1177/01617346221120070.
[67] Liu Z, Wen H, Zhu Z, et al. Diagnosis of significant liver fibrosis in patients with chronic hepatitis b using a deep learning-based data integration network. Hepatol Int 2022;16:526–36. https://doi.org/10.1007/s12072-021-10294-4.
[68] Feng X, Chen X, Dong C, et al. Multi-scale information with attention integration for classification of liver fibrosis in b-mode us image. Comput Methods Progr Biomed 2022;215:1–10. https://doi.org/10.1016/j.cmpb.2021.106598.

[69] Song JG, Zhang YZ, Cheng JL, et al. Non-invasive quantitative diagnosis of liver fibrosis with an artificial neural network. Neural Comput Appl 2022;34:6733–44. https://doi.org/10.1007/s00521-021-06257-3.
[70] Saito R, Koizumi N, Nishiyama Y, et al. Evaluation of ultrasonic fibrosis diagnostic system using convolutional network for ordinal regression. Int J Comput Assist Radiol Surg 2021;16:1969–75. https://doi.org/10.1007/s11548-021-02491-1.
[71] Ruan D, Shi Y, Jin L, et al. An ultrasound image-based deep multi-scale texture network for liver fibrosis grading in patients with chronic hbv infection. Liver Int 2021;41:2440–54. https://doi.org/10.1111/liv.14999.
[72] Brausch L, Tretbar S, Hewener H. Identification of advanced hepatic steatosis and fibrosis using ml algorithms on high-frequency ultrasound data in patients with non-alcoholic fatty liver disease. In: 2021 IEEE UFFC Latin America Ultrasonics Symposium (LAUS); 2021. p. 1–4. https://doi.org/10.1109/LAUS53676.2021.9639128.
[73] Borro P, Ziola S, Pasta A, et al. Hepatic elastometry and glissonian line in the assessment of liver fibrosis. Ultrasound Med Biol 2021;47:947–59. https://doi.org/10.1016/j.ultrasmedbio.2020.12.015.
[74] Zhou H, Wang K, Tian J, et al. The accurate non-invasive staging of liver fibrosis using deep learning radiomics based on transfer learning of shear wave elastography. Med Imag 2020 Ultrason Imag Tomogr 2020;11319:1–10. https://doi.org/10.1117/12.2549425.
[75] Xue L, Jiang Z, Fu T, et al. Transfer learning radiomics based on multimodal ultrasound imaging for staging liver fibrosis. Eur Radiol 2020;30:2973–83. https://doi.org/10.1007/s00330-019-06595-w.
[76] Lu X, Yang X, Sun J, et al. Fibrobox: a novel noninvasive tool for predicting significant liver fibrosis and cirrhosis in hbv infected patients. Biomark Res 2020;8:48. https://doi.org/10.1186/s40364-020-00215-2.
[77] Lee JH, Joo I, Kang TW, et al. Deep learning with ultrasonography: automated classification of liver fibrosis using a deep convolutional neural network. Eur Radiol 2020;30:1264–73. https://doi.org/10.1007/s00330-019-06407-1.
[78] Durot I, Akhbardeh A, Sagreiya H, et al. A new multimodel machine learning framework to improve hepatic fibrosis grading using ultrasound elastography systems from different vendors. Ultrasound Med Biol 2020;46:26–33. https://doi.org/10.1016/j.ultrasmedbio.2019.09.004.
[79] Drazinos P, Gatos I, Tsantis S, et al. A deep learning approach on cirrhosis diagnosis utilizing ultrasound b-mode images of segmented liver left lobes using liver biopsy as the gold standard. Med Phys 2020;47:E507. E507.
[80] Brattain L, Ozturk A, Telfer B, et al. Image processing pipeline for liver fibrosis classification using ultrasound shear wave elastography. Ultrasound Med Biol 2020;46:2667–76. https://doi.org/10.1016/j.ultrasmedbio.2020.05.016.
[81] Wang K, Lu X, Zhou H, et al. Deep learning radiomics of shear wave elastography significantly improved diagnostic performance for assessing liver fibrosis in chronic hepatitis b: a prospective multicentre study. Gut 2019;68:729. https://doi.org/10.1136/gutjnl-2018-316204.
[82] Li W, Huang Y, Zhuang B, et al. Multiparametric ultrasomics of significant liver fibrosis: a machine learning-based analysis. Eur Radiol 2019;29:1496–506. https://doi.org/10.1007/s00330-018-5680-z.
[83] Gatos I, Tsantis S, Spiliopoulos S, et al. Temporal stability assessment in shear wave elasticity images validated by deep learning neural network for chronic liver disease fibrosis stage assessment. Med Phys 2019;46:2298–309. https://doi.org/10.1002/mp.13521.
[84] Li D, Miao H, Li X, et al. Classification of diffuse liver diseases based on ultrasound images with multimodal features. In: 2019 IEEE International Instrumentation and Measurement Technology Conference (I2MTC). vol. 5; 2019. p. 5. https://doi.org/10.1109/i2mtc.2019.8827174.
[85] Acharya U, Raghavendra U, Koh J, et al. Automated detection and classification of liver fibrosis stages using contourlet transform and nonlinear features. Comput Methods Progr Biomed 2018;166:91–8. https://doi.org/10.1016/j.cmpb.2018.10.006.
[86] Xu Z, Liu X, Cheng X, et al. Diagnosis of cirrhosis stage via deep neural network. In: 2017 IEEE International Conference on Bioinformatics and Biomedicine (BIBM); 2017. p. 745–9. https://doi.org/10.1109/BIBM.2017.8217748.
[87] Meng D, Zhang L, Cao G, et al. Liver fibrosis classification based on transfer learning and fcnet for ultrasound images. IEEE Access 2017;5:5804–10. https://doi.org/10.1109/ACCESS.2017.2689058.
[88] Liu X, Song J, Wang S, et al. Learning to diagnose cirrhosis with liver capsule guided ultrasound image classification. Sensors 2017;17:1–11. https://doi.org/10.3390/s17010149.
[89] Lei B, Liu Y, Dong C, et al. Assessment of liver fibrosis in chronic hepatitis b via multimodal data. Neurocomputing 2017;253:169–76. https://doi.org/10.1016/j.neucom.2016.09.128.
[90] Alempijevic T, Zec S, Nikolic V, et al. Doppler ultrasonography combined with transient elastography improves the non-invasive assessment of fibrosis in patients with chronic liver diseases. Med Ultrasonogr 2017;19:7–15. https://doi.org/10.11152/mu-921.
[91] Yongshuai L, Qiong H, Jianwen L. A deep learning trial on transient elastography for assessment of liver fibrosis. In: 2018 IEEE International Ultrasonics Symposium (IUS). vol. 110; 2018. p. 1–4. https://doi.org/10.1109/ultsym.2018.8579992.
[92] Dadoun H, Rousseau A-L, de Kerviler E, et al. Deep learning for the detection, localization, and characterization of focal liver lesions on abdominal us images. Radiol Artif Intell 2022;4:e210110. https://doi.org/10.1148/ryai.210110.
[93] Turco S, Tiyarattanachai T, Ebrahimkheil K, et al. Interpretable machine learning for characterization of focal liver lesions by contrast-enhanced ultrasound. IEEE Trans Ultrason Ferroelectrics Freq Control 2022;69:1670–81. https://doi.org/10.1109/tuffc.2022.3161719.
[94] Zhang W-b, Hou S-z, Chen Y-l, et al. Deep learning for approaching hepatocellular carcinoma ultrasound screening dilemma: identification of alpha-fetoprotein-negative hepatocellular carcinoma from focal liver lesion found in high-risk patients. Front Oncol 2022;12:862297. https://doi.org/10.3389/fonc.2022.862297.
[95] Zhou J, Pan F, Li W, et al. Feature fusion for diagnosis of atypical hepatocellular carcinoma in contrast- enhanced ultrasound. IEEE Trans Ultrason Ferroelectrics Freq Control 2022;69:114–23. https://doi.org/10.1109/TUFFC.2021.3110590.
[96] Nishida N, Yamakawa M, Shiina T, et al. Artificial intelligence (ai) models for the ultrasonographic diagnosis of liver tumors and comparison of diagnostic accuracies between ai and human experts. J Gastroenterol 2022;57:309–21. https://doi.org/10.1007/s00535-022-01849-9.
[97] Zhou H, Jiang T, Li Q, et al. Us-based deep learning model for differentiating hepatocellular carcinoma (hcc) from other malignancy in cirrhotic patients. Front Oncol 2021;11:1–10. https://doi.org/10.3389/fonc.2021.672055.
[98] Xi I, Wu J, Guan J, et al. Deep learning for differentiation of benign and malignant solid liver lesions on ultrasonography. Abdominal Radiology 2021;46:534–43. https://doi.org/10.1007/s00261-020-02564-w.
[99] Wang W, Zhang J, Tian W, et al. Shear wave elastography-based ultrasomics: differentiating malignant from benign focal liver lesions. Abdom Radiol 2021;46:237–48. https://doi.org/10.1007/s00261-020-02614-3.
[100] Tiyarattanachai T, Apiparakoon T, Marukatat S, et al. Development and validation of artificial intelligence to detect and diagnose liver lesions from ultrasound images. PLoS One 2021;16:1–14. https://doi.org/10.1371/journal.pone.0252882.
[101] Ryu H, Shin S, Lee J, et al. Joint segmentation and classification of hepatic lesions in ultrasound images using deep learning. Eur Radiol 2021;31:8733–42. https://doi.org/10.1007/s00330-021-07850-9.
[102] Ren S, Li Q, Liu S, et al. Clinical value of machine learning-based ultrasomics in preoperative differentiation between hepatocellular carcinoma and intrahepatic cholangiocarcinoma: a multicenter study. Front Oncol 2021;11:749137. https://doi.org/10.3389/fonc.2021.749137.
[103] Yamakawa M, Shiina T, Tsugawa K, et al. Deep-learning framework based on a large ultrasound image database to realize computer-aided diagnosis for liver and breast tumors. In: 2021 IEEE International Ultrasonics Symposium (IUS). vol. 82; 2021. p. 1–4. https://doi.org/10.1109/ius52206.2021.9593518.
[104] Mitrea D, Badea R, Mitrea P, et al. Hepatocellular carcinoma automatic diagnosis within ceus and b-mode ultrasound images using advanced machine learning methods. Sensors 2021;21:1–31. https://doi.org/10.3390/s21062202.
[105] Marya NB, Powers PD, Fujii-Lau L, et al. Application of artificial intelligence using a novel eus-based convolutional neural network model to identify and distinguish benign and malignant hepatic masses. Gastrointest Endosc 2021;93:1121–30. https://doi.org/10.1016/j.gie.2020.08.024. e1121.
[106] Li W, Lv X, Zheng X, et al. Machine learning-based ultrasomics improves the diagnostic performance in differentiating focal nodular hyperplasia and atypical hepatocellular carcinoma. Front Oncol 2021;11:1–8. https://doi.org/10.3389/fonc.2021.544979.
[107] Hu H, Wang W, Chen L, et al. Artificial intelligence assists identifying malignant versus benign liver lesions using contrast-enhanced ultrasound. J Gastroenterol Hepatol 2021;36:2875–83. https://doi.org/10.1111/jgh.15522.
[108] Cheng M, Xian M, Tian W, et al. Rgb three-channel swe-based ultrasomics model: improving the efficiency in differentiating focal liver lesions. Front Oncol 2021;11:704218. https://doi.org/10.3389/fonc.2021.704218.
[109] Caleanu C, Sirbu C, Simion G. Deep neural architectures for contrast enhanced ultrasound (ceus) focal liver lesions automated diagnosis. Sensors 2021;21. https://doi.org/10.3390/s21124126.
[110] Yang Q, Wei J, Hao X, et al. Improving b-mode ultrasound diagnostic performance for focal liver lesions using deep learning: a multicentre study. EBioMedicine 2020;56:102777. https://doi.org/10.1016/j.ebiom.2020.102777.
[111] Sirbu C, Simion G, Caleanu C. Deep cnn for contrast-enhanced ultrasound focal liver lesions diagnosis. In: 2020 14th International Symposium on Electronics and Telecommunications (Isetc); 2020. p. 3–6.
[112] Peng Y, Lin P, Wu L, et al. Ultrasound-based radiomics analysis for preoperatively predicting different histopathological subtypes of primary liver cancer. Front Oncol 2020;10:1646. https://doi.org/10.3389/fonc.2020.01646.
[113] Nakashima T, Tsutsumi I, Takami H, et al. A study on liver tumor detection from an ultrasound image using deep learning. In: International Workshop on Advanced Imaging Technology (IWAIT) 2020. vol. 11515; 2020. p. 1–10. https://doi.org/10.1117/12.2566913.
[114] Mostafiz R, Rahman M, Islam A, et al. Focal liver lesion detection in ultrasound image using deep feature fusions and super resolution. Mach Learn Knowl Extract 2020;2:172–91. https://doi.org/10.3390/make2030010.
[115] Denis de Senneville B, Frulio N, Laumonier H, et al. Liver contrast-enhanced sonography: computer-assisted differentiation between focal nodular hyperplasia and inflammatory hepatocellular adenoma by reference to microbubble transport patterns. Eur Radiol 2020;30:2995–3003. https://doi.org/10.1007/s00330-019-06566-1.
[116] Brehar R, Mitrea D, Vancea F, et al. Comparison of deep-learning and conventional machine-learning methods for the automatic recognition of the hepatocellular carcinoma areas from ultrasound images. Sensors 2020;20. https://doi.org/10.3390/s20113085.
[117] Yamakawa M, Shiina T, Nishida N, et al. Computer aided diagnosis system developed for ultrasound diagnosis of liver lesions using deep learning. In: 2019

IEEE International Ultrasonics Symposium (IUS); 2019. p. 2330–3. https://doi.org/10.1109/ULTSYM.2019.8925698.
[118] Schmauch B, Herent P, Jehanno P, et al. Diagnosis of focal liver lesions from ultrasound using deep learning. Diag Intervent Imag 2019;100:227–33. https://doi.org/10.1016/j.diii.2019.02.009.
[119] Pan F, Huang Q, Li X. Classification of liver tumors with ceus based on 3d-cnn. In: 2019 IEEE 4th International Conference on Advanced Robotics and Mechatronics (ICARM 2019); 2019. p. 845–9. https://doi.org/10.1109/ICARM.2019.8834190.
[120] Mitrea D, Brehar R, Mitrea P, et al. The role of convolutional neural networks in the automatic recognition of the hepatocellular carcinoma, based on ultrasound images. In: 6th International Conference on Advancements of Medicine and Health Care Through Technology, Meditech 2018. vol. 71; 2019. p. 169–75. https://doi.org/10.1007/978-981-13-6207-1_27.
[121] Brehar R, Mitrea D, Nedevschi S, et al. Hepatocellular carcinoma recognition in ultrasound images using textural descriptors and classical machine learning. In: 2019 IEEE 15th International Conference on Intelligent Computer Communication and Processing (Iccp 2019); 2019. p. 491–7. https://doi.org/10.1109/ICCP48234.2019.8959755.
[122] Yao Z, Dong Y, Wu G, et al. Preoperative diagnosis and prediction of hepatocellular carcinoma: radiomics analysis based on multi-modal ultrasound images. BMC Cancer 2018;18:1089. https://doi.org/10.1186/s12885-018-5003-4.
[123] Ta C, Kono Y, Eghtedari M, et al. Focal liver lesions: computer-aided diagnosis by using contrast-enhanced us cine recordings. Radiology 2018;286:1062–71. https://doi.org/10.1148/radiol.2017170365.
[124] Guo L, Wang D, Qian Y, et al. A two-stage multi-view learning framework based computer-aided diagnosis of liver tumors with contrast enhanced ultrasound images. Clin Hemorheol Microcirc 2018;69:343–54. https://doi.org/10.3233/CH-170275.
[125] Acharya U, Koh J, Hagiwara Y, et al. Automated diagnosis of focal liver lesions using bidirectional empirical mode decomposition features. Comput Biol Med 2018;94:11–8. https://doi.org/10.1016/j.compbiomed.2017.12.024.
[126] Kondo S, Takagi K, Nishida M, et al. Computer-aided diagnosis of focal liver lesions using contrast-enhanced ultrasonography with perflubutane microbubbles. IEEE Trans Med Imag 2017;36:1427–37. https://doi.org/10.1109/TMI.2017.2659734.
[127] Hassan T, Elmogy M, Sallam E. Diagnosis of focal liver diseases based on deep learning technique for ultrasound images. Arabian J Sci Eng 2017;42:3127–40. https://doi.org/10.1007/s13369-016-2387-9.
[128] Noble JA. Ultrasound image segmentation and tissue characterization. Proc Inst Mech Eng Part H J Eng Med 2010;224:307–16. https://doi.org/10.1243/09544119jeim604.
[129] Noble JA, Boukerroui D. Ultrasound image segmentation: a survey. IEEE Trans Med Imag 2006;25:987–1010. https://doi.org/10.1109/tmi.2006.877092.
[130] Brattain LJ, Telfer BA, Dhyani M, et al. Machine learning for medical ultrasound: status, methods, and future opportunities. Abdom Radiol 2018;43:786–99. https://doi.org/10.1007/s00261-018-1517-0.
[131] Jing X, Chen K, Xiangdong Y, et al. Adaptive level set method for segmentation of liver tumors in minimally invasive surgery using ultrasound images. In: 2007 1st International Conference on Bioinformatics and Biomedical Engineering; 2007. p. 1091–4. https://doi.org/10.1109/ICBBE.2007.282.
[132] Ryu H, Shin SY, Lee JY, et al. Joint segmentation and classification of hepatic lesions in ultrasound images using deep learning. Eur Radiol 2021;31:8733–42. https://doi.org/10.1007/s00330-021-07850-9.
[133] Mamuleanu M, Serbanescu M, Urhut CM, et al. Liver lesion segmentation in contrast-enhanced ultrasound using deep learning algorithms. Ultrasound Med Biol 2022;48:S6. https://doi.org/10.1016/j.ultrasmedbio.2022.04.035.
[134] Mishra D, Chaudhury S, Sarkar M, et al. Segmentation of vascular regions in ultrasound images: a deep learning approach. In: 2018 IEEE International Symposium on Circuits and Systems (ISCAS); 2018. p. 1–5. https://doi.org/10.1109/ISCAS.2018.8351049.
[135] Mishra D, Chaudhury S, Sarkar M, et al. Ultrasound image segmentation: a deeply supervised network with attention to boundaries. IEEE Trans Biomed Eng 2019;66:1637–48. https://doi.org/10.1109/tbme.2018.2877577.
[136] Wei W, Xu H, Alpers J, et al. Fast registration for liver motion compensation in ultrasound-guided navigation. In: 2019 IEEE 16th International Symposium on Biomedical Imaging (ISBI 2019); 2019. p. 1132–6. https://doi.org/10.1109/ISBI.2019.8759464.
[137] Thomson BR, Smit JN, Ivashchenko OV, et al. Mr-to-us registration using multiclass segmentation of hepatic vasculature with a reduced 3d u-net. In: Medical Image Computing and Computer Assisted Intervention - MICCAI 2020. 23rd International Conference. Proceedings. Lecture Notes in Computer Science. vol. 44; 2020. p. 275–84. https://doi.org/10.1007/978-3-030-59716-0_27.
[138] Montana-Brown N, Ramalhinho J, Allam M, et al. Vessel segmentation for automatic registration of untracked laparoscopic ultrasound to ct of the liver. Int J Comput Assist Radiol Surg 2021;16:1151–60. https://doi.org/10.1007/s11548-021-02400-6.
[139] Wei W, Rak M, Alpers J, et al. Towards fully automatic 2d us to 3d ct/mr registration: a novel segmentation-based strategy. In: IEEE 17th International Symposium on Biomedical Imaging (ISBI); 2020. p. 433–7. https://doi.org/10.1109/ISBI45749.2020.9098379.
[140] Wei W, Xu H, Alpers J, et al. A deep learning approach for 2d ultrasound and 3d ct/mr image registration in liver tumor ablation. Comput Methods Progr Biomed 2021;206:1–10. https://doi.org/10.1016/j.cmpb.2021.106117.
[141] Rethy A, Langa T, Marvik R. Laparoscopic ultrasound for hepatocellular carcinoma and colorectal liver metastasis: an overview. Surg Laparosc Endosc Percutaneous Tech 2013;23:135–44. https://doi.org/10.1097/SLE.0b013e31828a0b9a.
[142] Ramalhinho J, Tregidgo HFJ, Gurusamy K, et al. Registration of untracked 2d laparoscopic ultrasound to ct images of the liver using multi-labelled content-based image retrieval. IEEE Trans Med Imag 2021;40:1042–54. https://doi.org/10.1109/tmi.2020.3045348.
[143] Huang P, Su L, Chen S, et al. 2d ultrasound imaging based intra-fraction respiratory motion tracking for abdominal radiation therapy using machine learning. Phys Med Biol 2019;64:1–11. https://doi.org/10.1088/1361-6560/ab33db.
[144] Shepard AJ, Wang B, Foo TKF, et al. A block matching based approach with multiple simultaneous templates for the real-time 2d ultrasound tracking of liver vessels. Med Phys 2017;44:5889–900. https://doi.org/10.1002/mp.12574.
[145] Ozkan E, Tanner C, Kastelic M, et al. Robust motion tracking in liver from 2d ultrasound images using supporters. Int J Comput Assist Radiol Surg 2017;12:941–50. https://doi.org/10.1007/s11548-017-1559-8.
[146] Imaizumi T, Kondo R, Kusahara K, et al. Deep learning based 3-dimensional liver motion estimation using 2-dimensional ultrasound images. In: IEEE International Conference on Cyborg and Bionic Systems (CBS); 2019. p. 184–90. https://doi.org/10.1109/CBS46900.2019.9114447.
[147] Yagasaki S, Koizumi N, Nishiyama Y, et al. Estimating 3-dimensional liver motion using deep learning and 2-dimensional ultrasound images. Int J Comput Assist Radiol Surg 2020;15:1989–95. https://doi.org/10.1007/s11548-020-02265-1.
[148] Ning G, Zhang X, Liao H. Autonomic robotic ultrasound imaging system based on reinforcement learning. IEEE Trans Biomed Eng 2021;68:2787–97. https://doi.org/10.1109/tbme.2021.3054413.
[149] Kuwahara T, Hara K, Mizuno N, et al. Usefulness of deep learning analysis for the diagnosis of malignancy in intraductal papillary mucinous neoplasms of the pancreas. Clin Transl Gastroenterol 2019;10:8. https://doi.org/10.14309/ctg.0000000000000045.